The Abdus Salam
International Centre
for Theoretical Physics

United Nations
Educational, Scientific and
Cultural Organization

IAEA
International Atomic Energy Agency

2495-08

Joint ICTP-IAEA Workshop on Nuclear Data for Analytical Applications

21 - 25 October 2013

Fundamentals of the Particle Induced Gamma-ray Emission (PIGE) technique, experimental procedures and examples of PIGE analysis

Massimo Chiari
I.N.F.N. Florence

Strada Costiera, 11 - 34151 - Trieste - Italy • Tel. +39 0402240111 • Fax. +39 040224163 • sci_info@ictp.it • www.ictp.it
ICTP is governed by UNESCO, IAEA, and Italy, and it is a UNESCO Category 1 Institute

Fundamentals of the Particle Induced Gamma-ray Emission (PIGE) technique, experimental procedures and examples of PIGE analysis

Massimo Chiari / *I.N.F.N. Florence*

chiari@fi.infn.it

max0068

INFN LABEC Laboratorio di Tecniche Nucleari per i Beni Culturali - Firenze

Joint ICTP-IAEA Workshop on Nuclear Data for Analytical Applications,
Trieste - Italy, 21 - 25 October 2013

Outline

- Fundamentals of PIGE technique
- Elemental bulk analysis by PIGE
- Depth profiling by PIGE
- Examples of PIGE bulk analysis (thick targets, thin targets)
- Essential bibliography

Ion Beam Analysis techniques

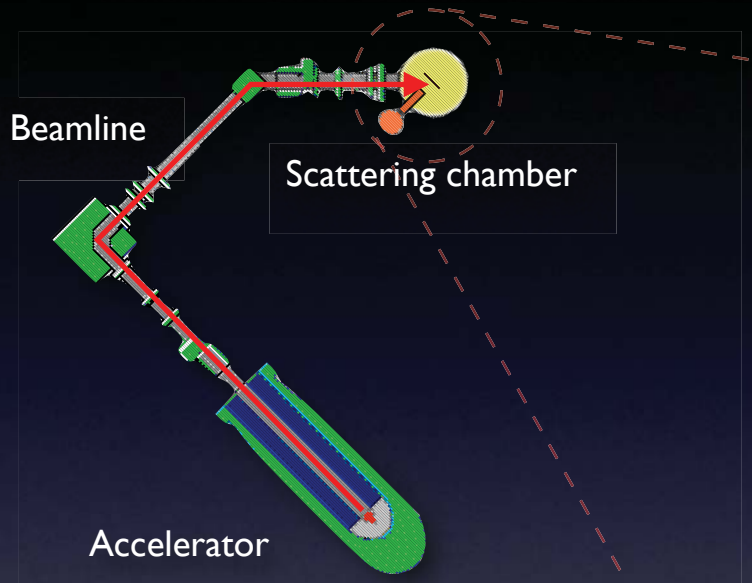

Beam IN	Beam OUT	Analytical technique
ion	ion	RBS, EBS*, NRA, PESA
ion	target	ERDA, SIMS, SNMS
ion	X-ray	PIXE
ion	Gamma-ray	PIGE, Activation Analysis
ion	hv	Ionoluminescence (IL)

* EBS is the general extension of RBS at higher energies, where the elastic scattering cross section is no longer Rutherford

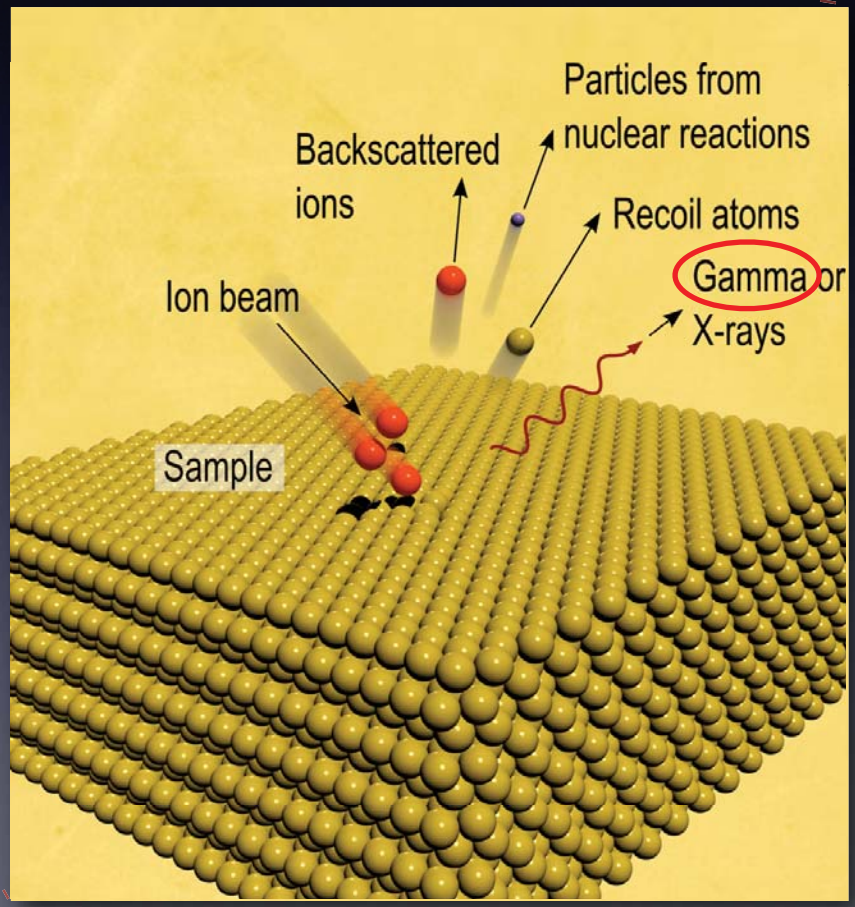

General features of IBA

- Multielemental
- Quantitative analysis
- High sensitivity (1-100 ppm in at/cm^3; 10^{11}-10^{12} in at/cm^2)
- Surface analysis (10 Å - 10 µm)
- Depth profiling
- Non-destructive
- No sample pre-treatment
- Microanalysis (lateral resolution <1 µm)
- 2D mapping

PIGE technique basics

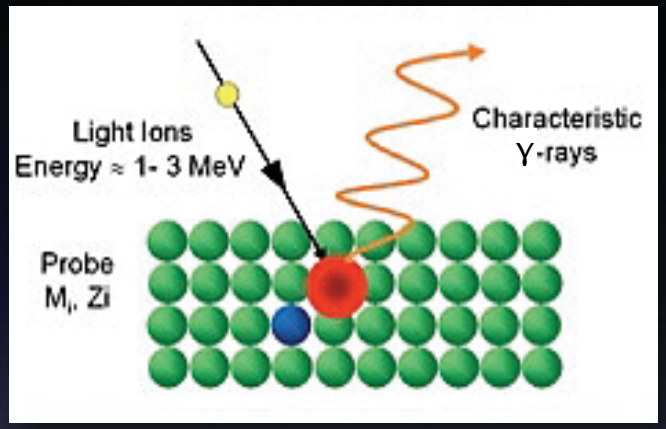

- For low-Z target elements, the incident beam particles can reach closer to the target nuclei (weaker Coulomb repulsion) and the short-range nuclear interaction comes into play.
- The target nucleus can be excited and the de-excitation of the nucleus occurs through the **prompt*** emission of a gamma-ray.

* the emission occurs during the irradiation (short life time of the level, < 1 sec).

PIGE technique basics

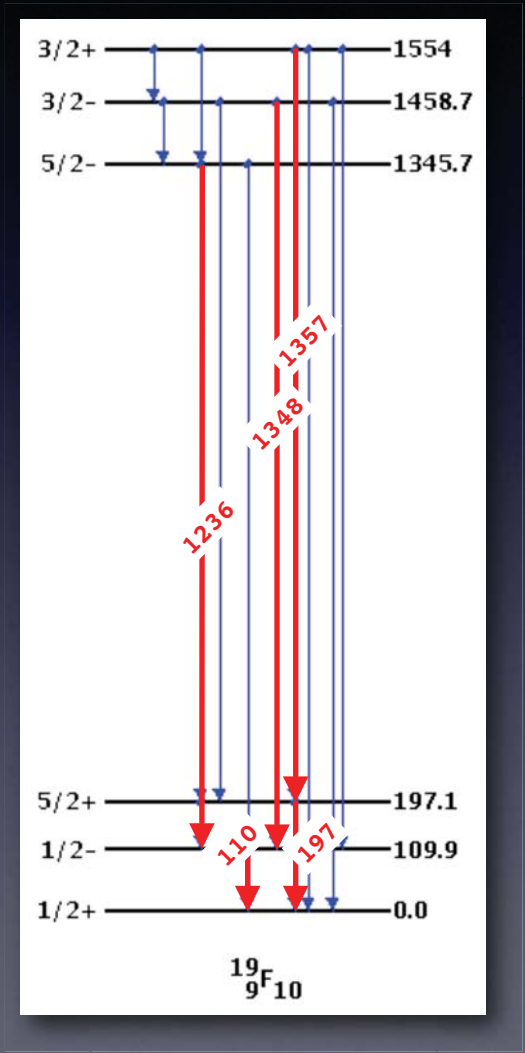

- Nuclear energy levels are specific for each isotope, hence the gamma-ray energies, are a characteristic "fingerprint" of every single isotope.
- The detection of gamma-ray energies allows to identify and quantify the low-Z isotopes in the target sample.

Nuclear reactions with prompt emission of gamma -rays

Radiative capture (direct reaction)	$a + A \rightarrow B^* \rightarrow B + \gamma$	$^{27}Al(p,\gamma)^{28}Si$
Inelastic scattering	$a + A \rightarrow A^* + a'$ $\searrow$ $A + \gamma$	$^{27}Al(p,p'\gamma)^{27}Al$
Rearrangement collisions	$a + A \rightarrow C^* + c$ $\searrow$ $C + \gamma$	$^{27}Al(p,\alpha\gamma)^{24}Mg$

List of proton-induced reactions

Element	E_γ (keV)	Nuclear origin	Transition	Detection limit (%)	Possible interferences
Li	429	$^{7}Li(p,n\gamma)^{7}Be$	429 → 0	0.01	As(427), B(429)
	478	$^{7}Li(p,p'\gamma)^{7}Li$	478 → 0	5×10^{-4}	Be(478), Mn(478)
Be	415	$Be^{9}(p,\gamma)B^{10}$	2154 → 1740		Ag(415)
	718	$Be^{9}(p,\gamma)B^{10}$	718 → 0		B(718)
	1023	$Be^{9}(p,\gamma)B^{10}$	1740 → 718		Ti(1022)
	1437	$Be^{9}(p,\gamma)B^{10}$	3590 → 2150		
	3562	$Be^{9}(p,\alpha\gamma)Li^{6}$	3562 → 0	0.1	
B	429	$^{10}B(p,\alpha)^{7}Be$	429 → 0		As(427), Li(429)
	478	$^{10}B(p,\alpha\gamma)^{7}Be \rightarrow ^{7}Li$	478 → 0		Li(478), Mn(478)
	718	$^{10}B(p,p'\gamma)^{10}B$	718 → 0		Be(718)
	2124	$^{10}B(p,p'\gamma)^{10}B$	2124 → 0	5×10^{-3}	
	4433	$^{11}B(p,\gamma)^{12}C$	4433 → 0		N(4433)

List of proton-induced reactions

Element	E_γ (keV)	Nuclear origin	Transition	Detection limit (%)	Possible interferences
C	2357	$^{12}C(p,\gamma)^{13}N$	2357 → 0	1	
N	1400	$^{14}N(p,\gamma)^{15}O$			Cr(1400)
	4433	$^{15}N(p,\alpha\gamma)^{12}C$	4433 → 0		B(4433)
O	110	$^{18}O(p,\gamma)^{19}F$	110 → 0		F(110), W(111)
	197	$^{16}O(p,\gamma)^{19}F$	197 → 0		F(197), Co(197), Ni(197), Ga(197), Ti(199), Ge(199)
	496	$^{16}O(p,\gamma)^{17}F$	496 → 0	5	Ga(493)
F	110	$^{19}F(p,p'\gamma)^{19}F$	110 → 0	2×10^{-4}	O(110), W(111)
	197	$^{19}F(p,p'\gamma)^{19}F$	197 → 0	5×10^{-5}	Co(197), Ni(197), Ga(197) Ti(199), Ge(199), O(197)
Na	439	$^{23}Na(p,p'\gamma)^{23}Na$	439 → 0	10^{-3}	Se(439)
	1368	$^{23}Na(p,\gamma)^{24}Mg$	1368 → 0		Mg(1368), Al(1368)
	1633	$^{23}Na(p,\alpha\gamma)^{20}Ne$	1633 → 0		

List of proton-induced reactions

Element	E_γ (keV)	Nuclear origin	Transition	Detection limit (%)	Possible interferences
Mg	170	$^{26}Mg(p,\gamma)^{27}Al$	1014 → 844		Al(170)
	390	$^{25}Mg(p,p'\gamma)^{25}Mg$	975 → 585		
	585	$^{25}Mg(p,p'\gamma)^{25}Mg$	585 → 0	5×10^{-3}	
	844	$^{26}Mg(p,\gamma)^{27}Al$	844 → 0		Al(844)
	975	$^{25}Mg(p,p'\gamma)^{25}Mg$	975 → 0		
	1014	$^{26}Mg(p,\gamma)^{27}Al$	1014 → 0		Ti(1012), Al(1014)
	1368	$^{24}Mg(p,p'\gamma)^{24}Mg$	1368 → 0		Na(1368), Al(1368)
Al	170	$^{27}Al(p,p'\gamma)^{27}Al$	1014 → 844		Mg(170)
	844	$^{27}Al(p,p'\gamma)^{27}Al$	844 → 0	2×10^{-3}	Mg(844)
	1014	$^{27}Al(p,p'\gamma)^{27}Al$	1014 → 0	5×10^{-3}	Ti(1012), Mg(1014)
	1368	$^{27}Al(p,\alpha\gamma)^{24}Mg$	1368 → 0		Na(1368), Mg(1368)
	1779	$^{27}Al(p,\gamma)^{28}Si$	1779 → 0		Si(1779), P(1779)
Si	1273	$^{29}Si(p,p'\gamma)^{29}Si$	1273 → 0	3	
	1779	$^{28}Si(p,p'\gamma)^{28}Si$	1779 → 0		Al(1779), P(1779)

Interaction of gamma-rays with matter

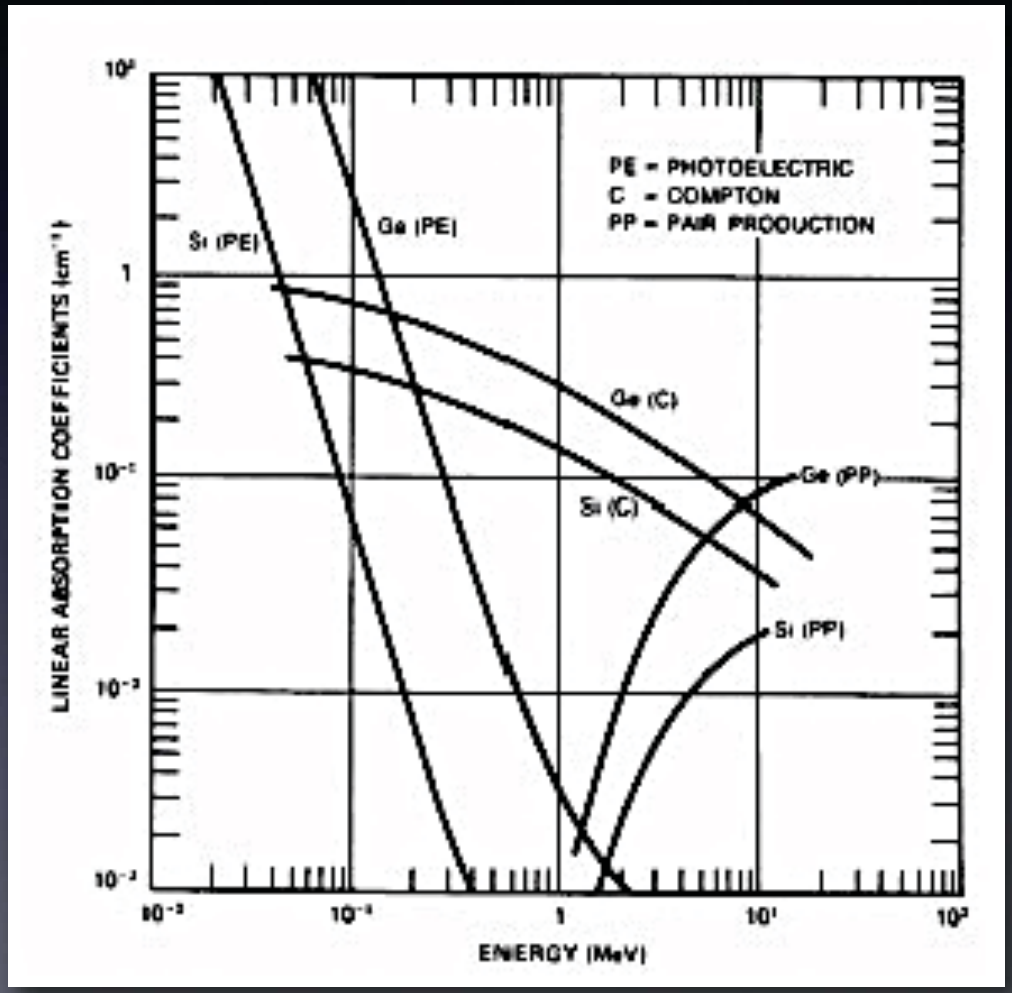

$$\sigma_{\text{photo}} \propto \frac{Z^4}{(h\nu)^3}$$

$$\sigma_{\text{Compton}} \propto \frac{Z}{(h\nu)^2}$$

$$\sigma_{\text{pair}} \propto Z^2 \ln(h\nu)$$

Detector response

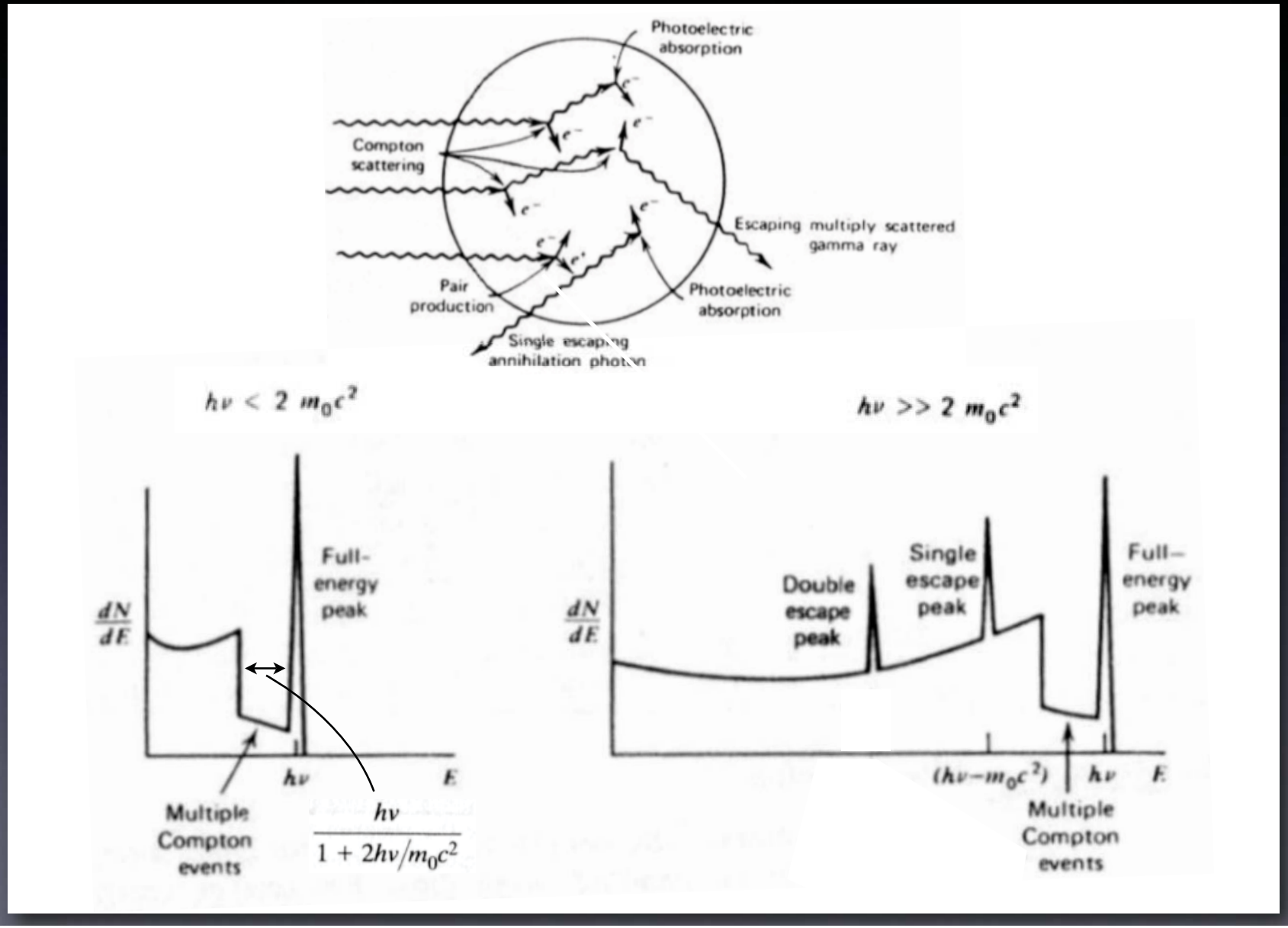

Detector response

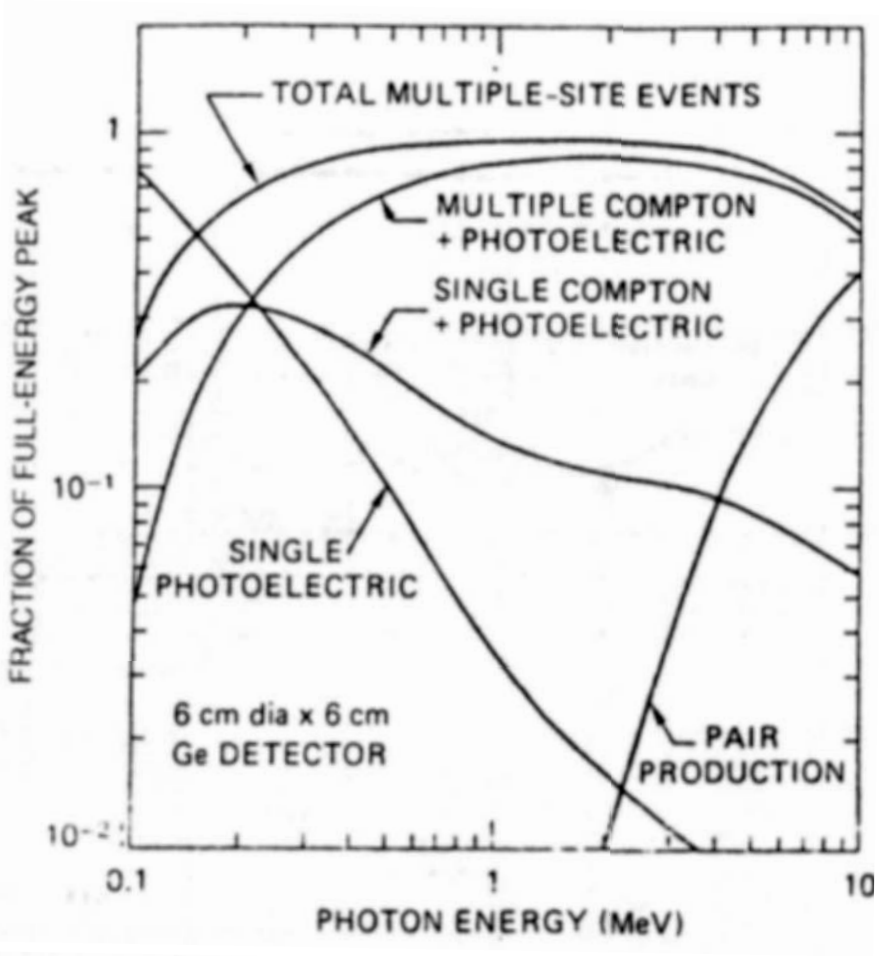

Figure 12.16 Fractions of the full-energy peak contributed by different energy loss mechanisms in a 6 cm × 6 cm coaxial HPGe detector, as predicted by Monte Carlo simulation. Absorption of the gamma-ray photon in a single photoelectric interaction predominates only for energies below about 140 keV. (From Roth et al.[43])

Detector efficiency

In order to measure absolute intensities, a calibration of the absolute detection efficiency in necessary, using calibration radioactive sources which span the energy region of interest.
Attention must be paid to the source-detector geometry and to the size of the radioactive source

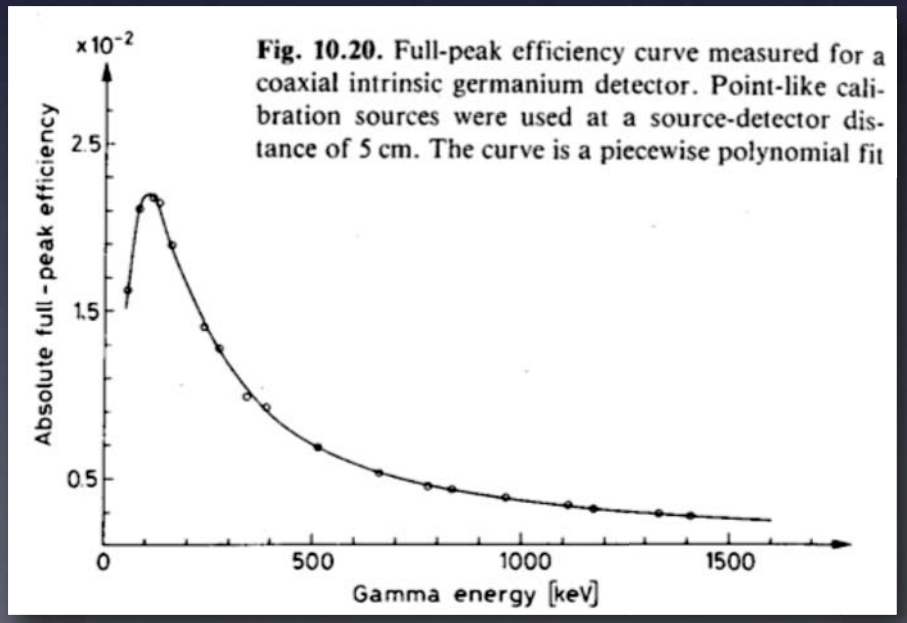

Fig. 10.20. Full-peak efficiency curve measured for a coaxial intrinsic germanium detector. Point-like calibration sources were used at a source-detector distance of 5 cm. The curve is a piecewise polynomial fit

In most cases the *full peak efficiency* (i.e. the efficiency for photoelectric conversion) is desired.

$$FPE = \frac{\textit{total yield in the photopeak}}{\textit{total output of the source}}$$

Examples of PIGE spectra

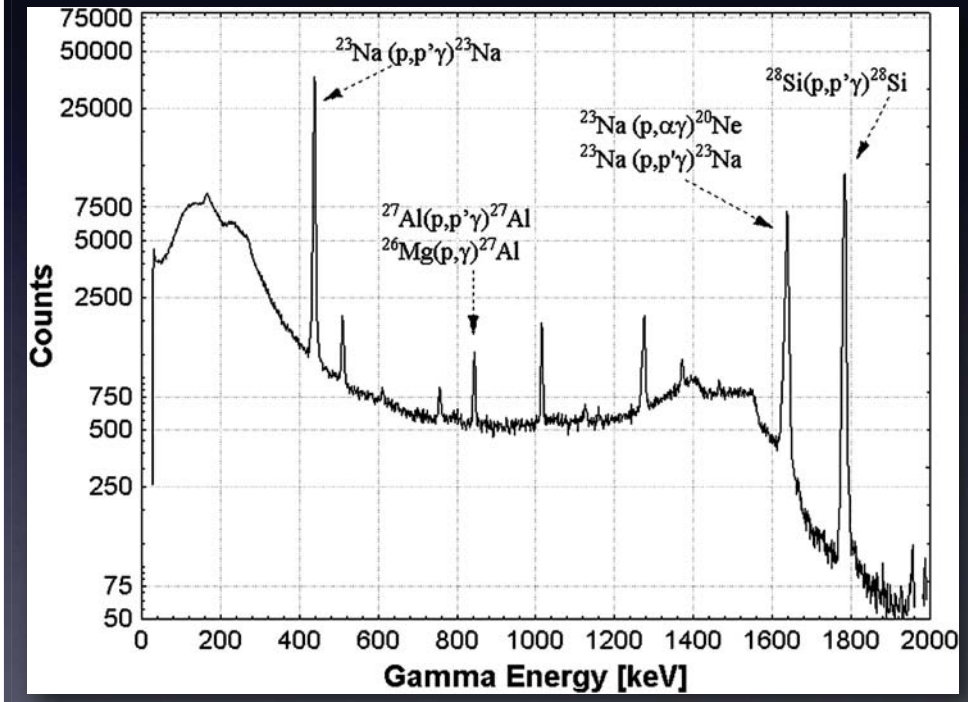

Soda-lime glass

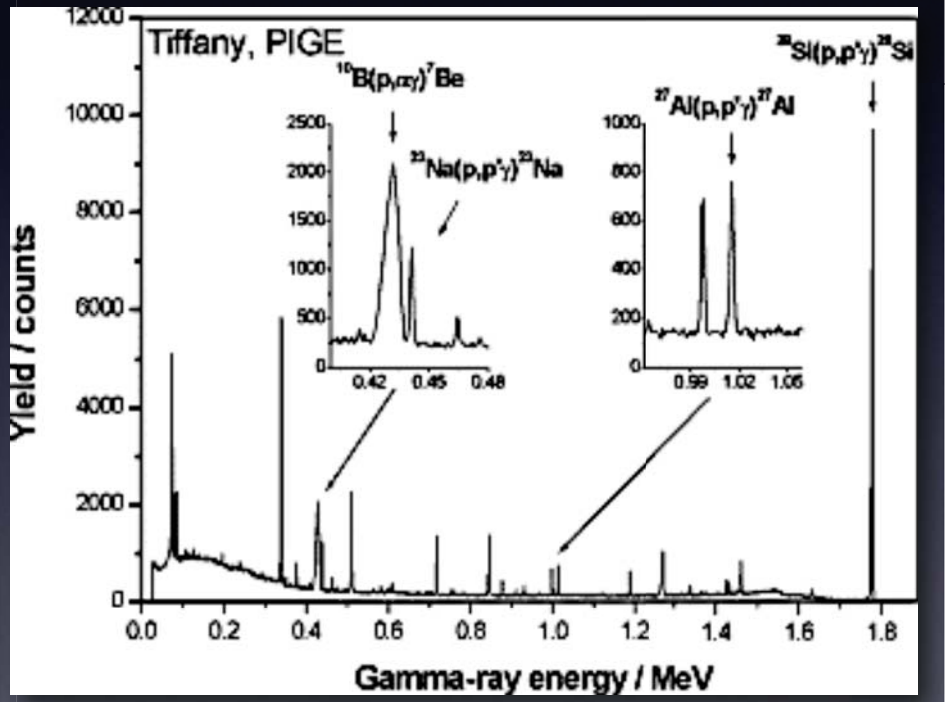

Boro-silicate glass

Broadening of gamma-ray lines

Doppler effect

$$E_\gamma = E'_\gamma \cdot (1 + v/c \cdot \cos\theta)$$

- the recoiling nucleus decays while moving
- high speed of the recoiling nucleus
- short life time of the transition (< 10^{-14} s)

Resonance width

Neutron detection

- produced by (p,n) or (α,n) reactions
- peaks appear in the low energy region (< 1 MeV)

Doppler broadening of gamma-ray lines

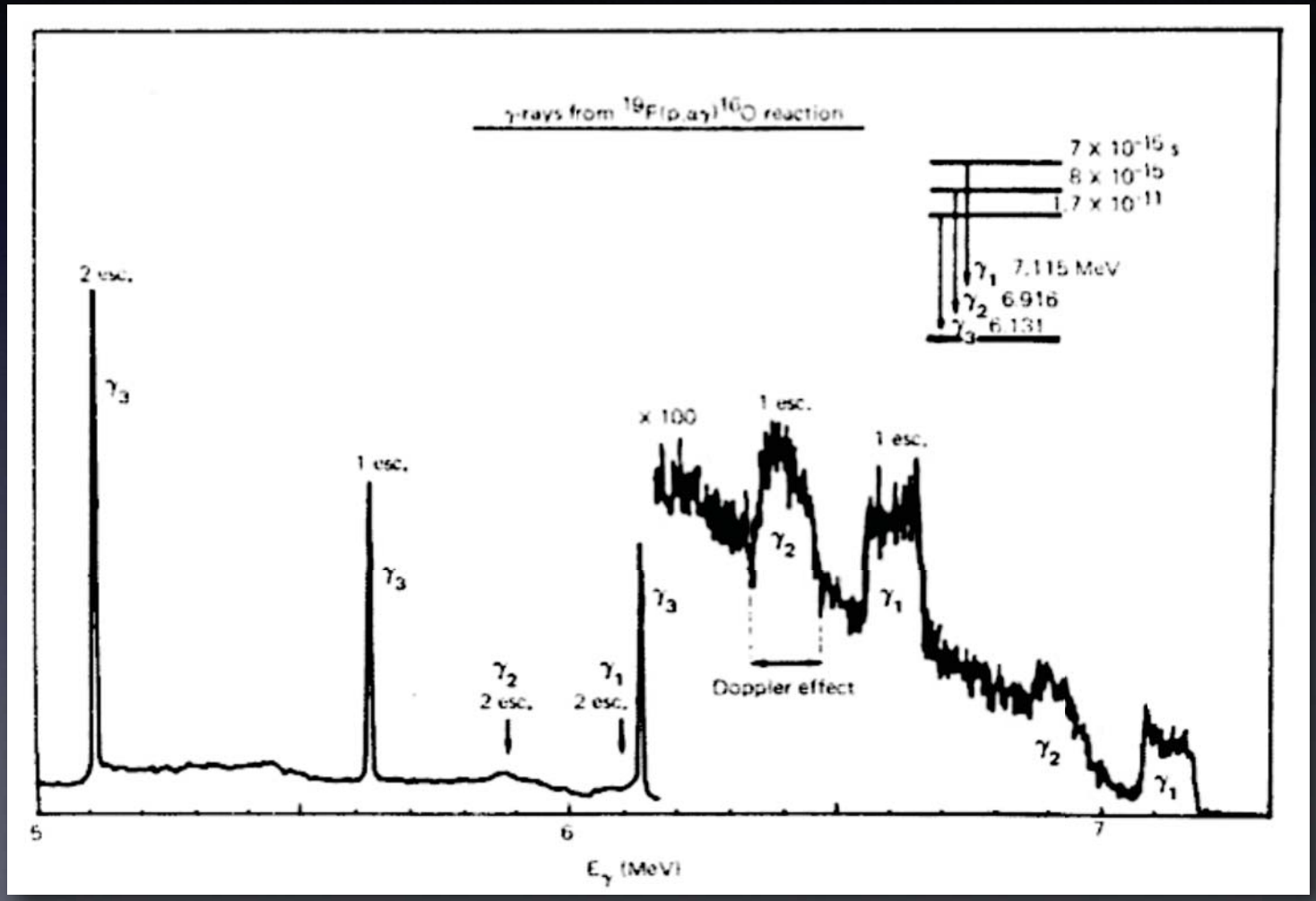

PIGE cross sections

The cross sections are the superimposition of resonances (Breit-Wigner) on a continuum due to direct nuclear reactions

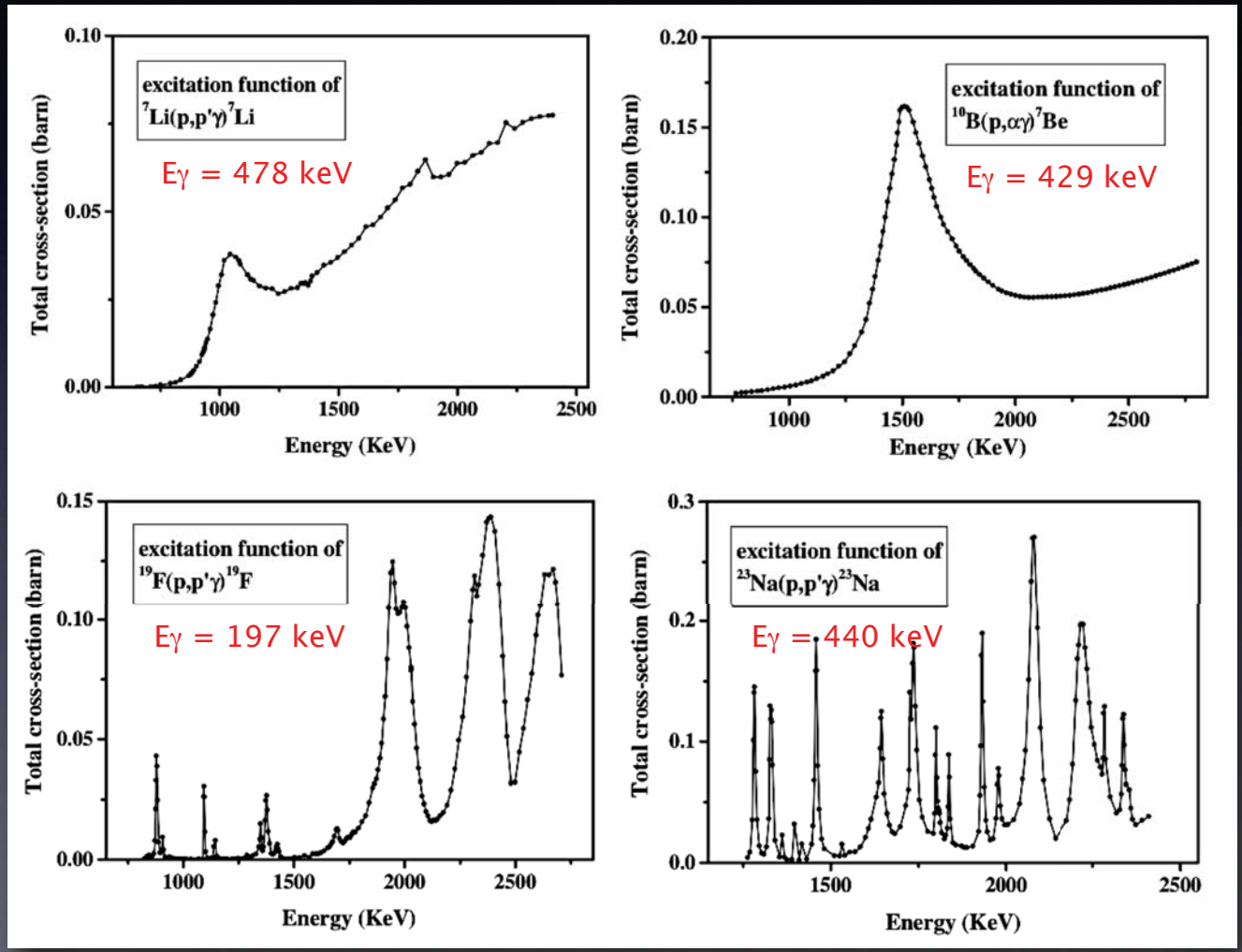

PIGE analysis scheme

Resonant PIGE	Depth profiling
Non-resonant PIGE	Bulk analysis

Which detector can be used?

Scintillators (NaI, BGO, LaBr3...)

- Depth profiling
- High efficiency
- Energy resolution is not critical

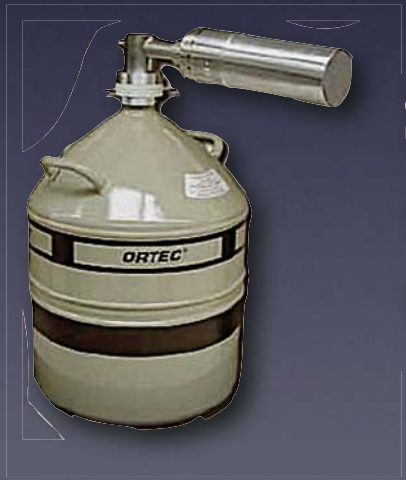

Semiconductors (HPGe, Ge(Li))

- Bulk analysis
- High energy resolution

Spectra obtained with different detectors

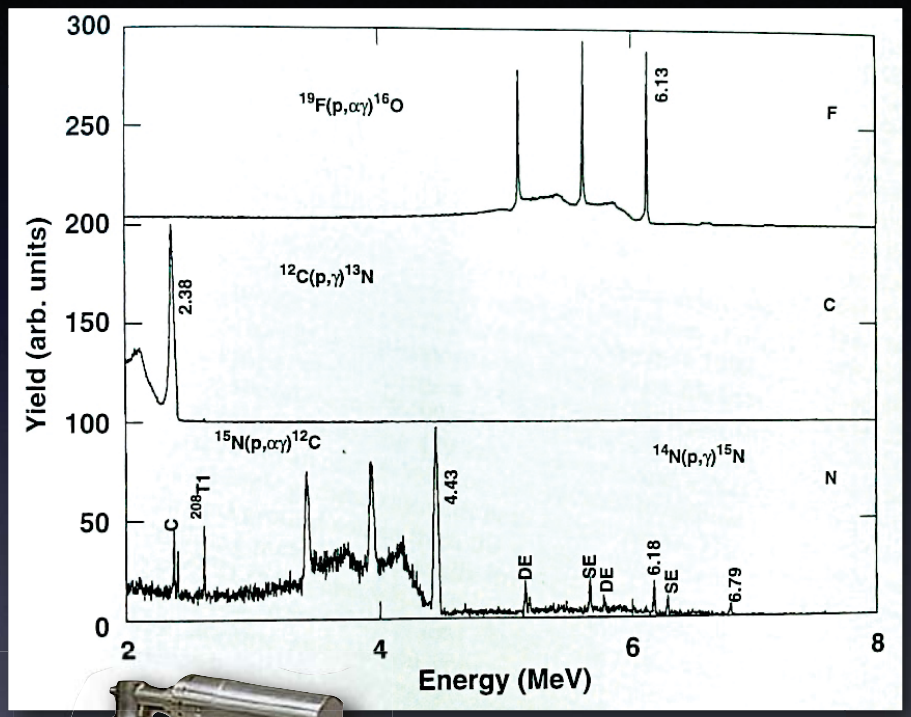

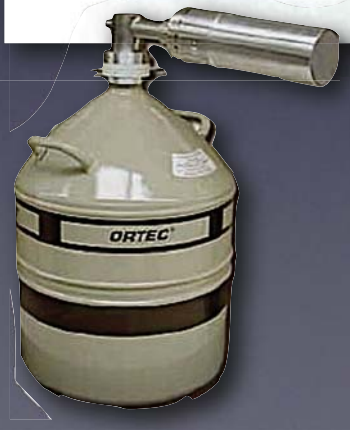

Ge(Li)

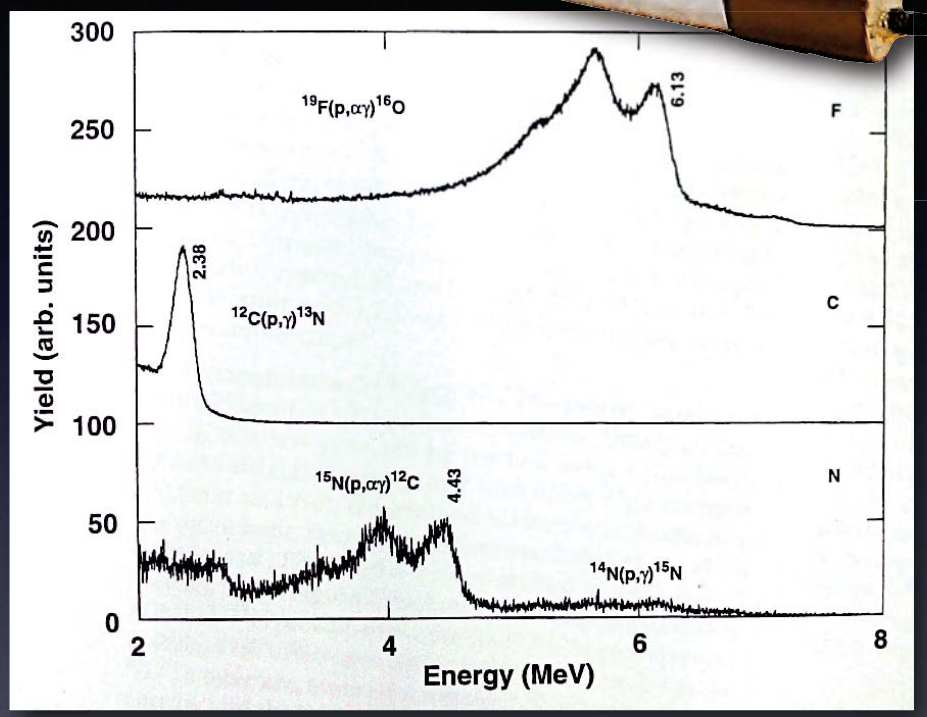

NaI(Tl)

PIGE bulk analysis

PIGE elemental analysis

The elemental concetrations (N_T) are obtained from measured quantities (i.e. gamma-ray peak areas) using physical models implementing the sample structure and the physical microscopic data and processes:

$$Y_\gamma(E_0,\theta) = \varepsilon_{\text{abs}}(E_\gamma)\cdot N_p \cdot \int_0^{E_0} N_T \cdot \sigma(E_0,\theta)/S(E)\,\mathrm{d}E$$

The principal needed microscopic data are **stopping powers** and **differential cross sections** of the interaction (as well as the detector absolute efficiency)

PIGE bulk analysis of thick targets

- (Semi-)Quantitative determination of light elements like Na, Al or Si in infinitely thick targets
- The unknown elemental concentrations are typically deduced by comparing the gamma-ray yields with those of thick standards of similar composition, without the detailed knowledge of the cross section
- The crucial point is the difference between the stopping power of the unknown sample and that of the standard

Thick-target gamma-ray yields

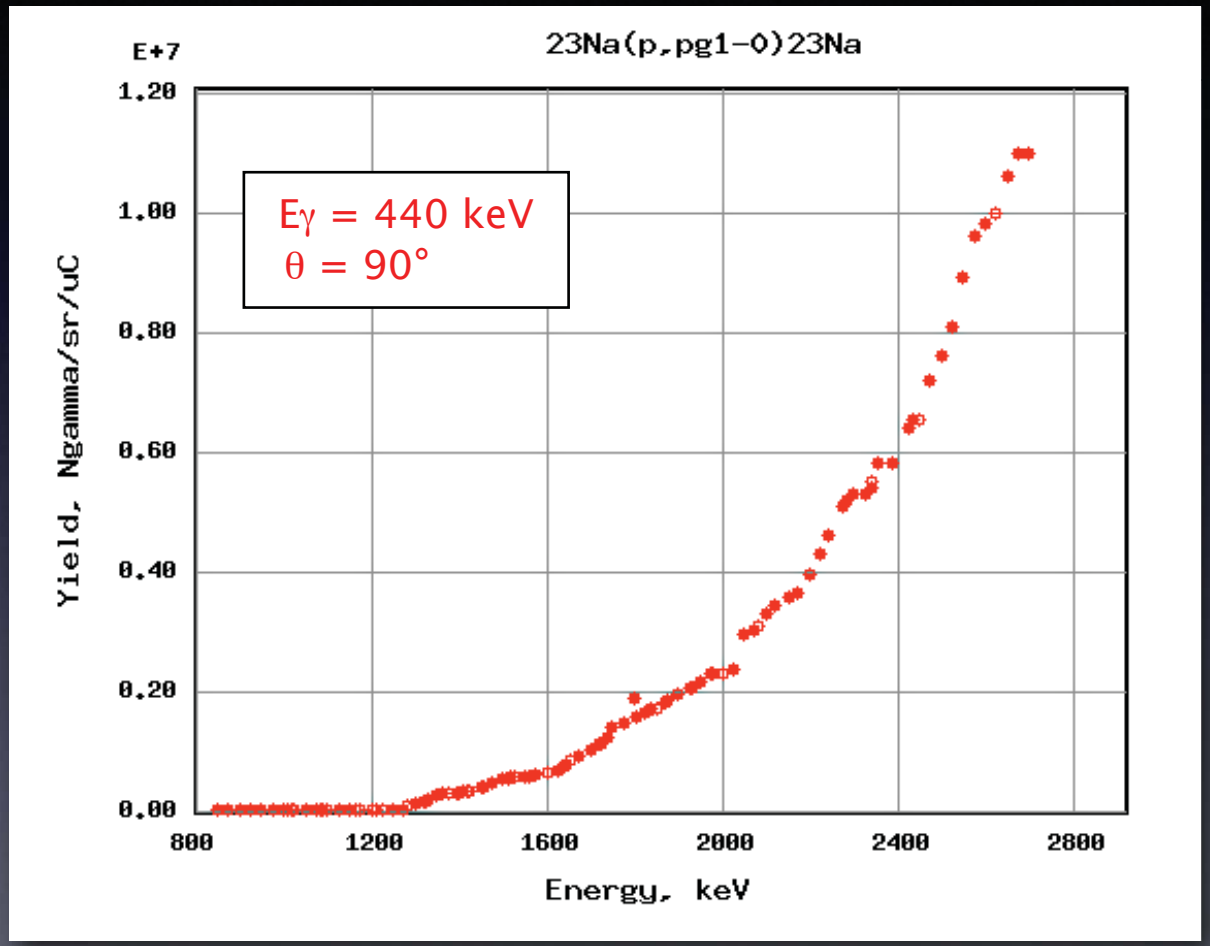

PIGE quantitative analysis: comparison with thick standards

$$C_{samp} = C_{std} \cdot Y_{samp}(E_0)/Y_{std}(E_0) \cdot S_{samp}(E_{½})/S_{rif}(E_{½})$$

$E_{½}$ such as:

$$Y(E_0) = 2 \cdot Y(E_{½})$$

The "$E_{½}$" method is valid as long as the excitation function varies slowly with the energy

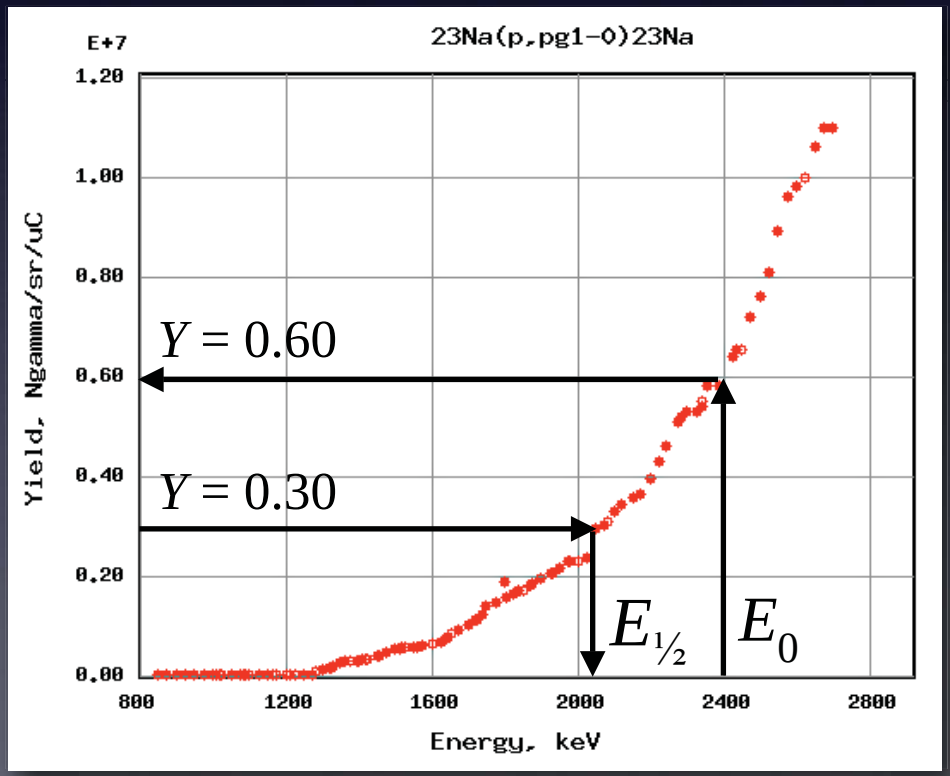

Identification of lapis-lazuli pigment in paint layers

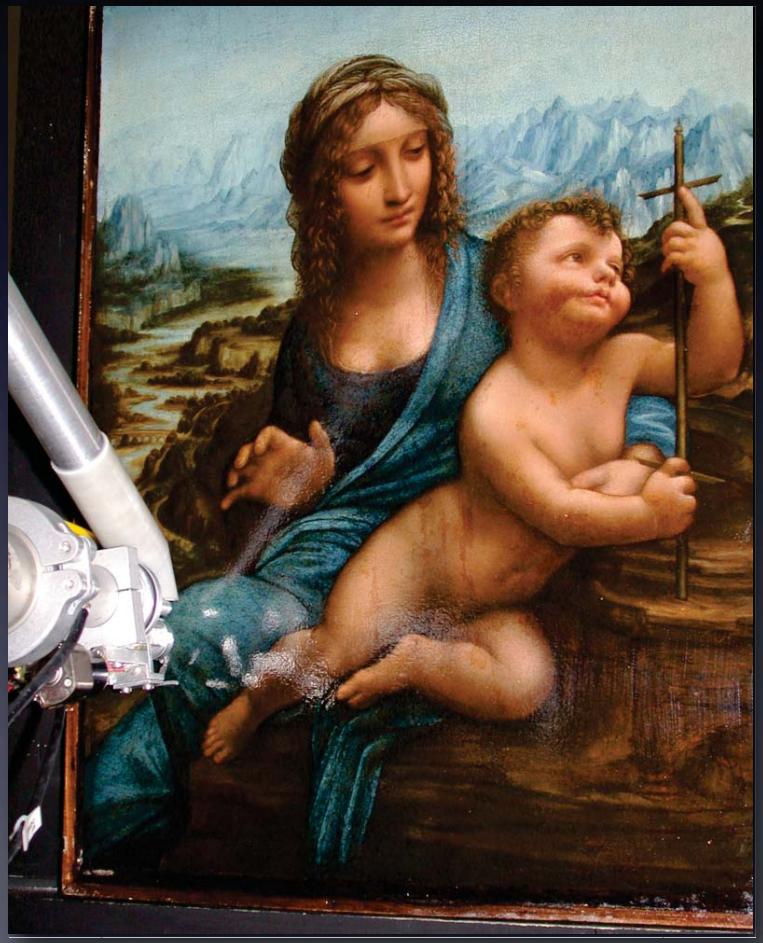

"Maddonna dei fusi", Leonardo da Vinci (1501)

Lapis-lazuli is a blue pigment, mainly composed of lazurite ($3Na_2O \cdot 3Al_2O_3 \cdot 6SiO_2 \cdot 2Na_2S$)

The possibility of identifying lapis-lazuli by PIXE in canvas and wood paintings is limited by:

- *low-energy X-rays absorption in the varnish and in the paint layer itself*
- *signal interference from other pigments*

Lapis-lazuli pigment in paint layers

PIXE spectra

PIGE spectra

Original

Blue pigment mixed with Lead white (Ca and Fe from the varnish)

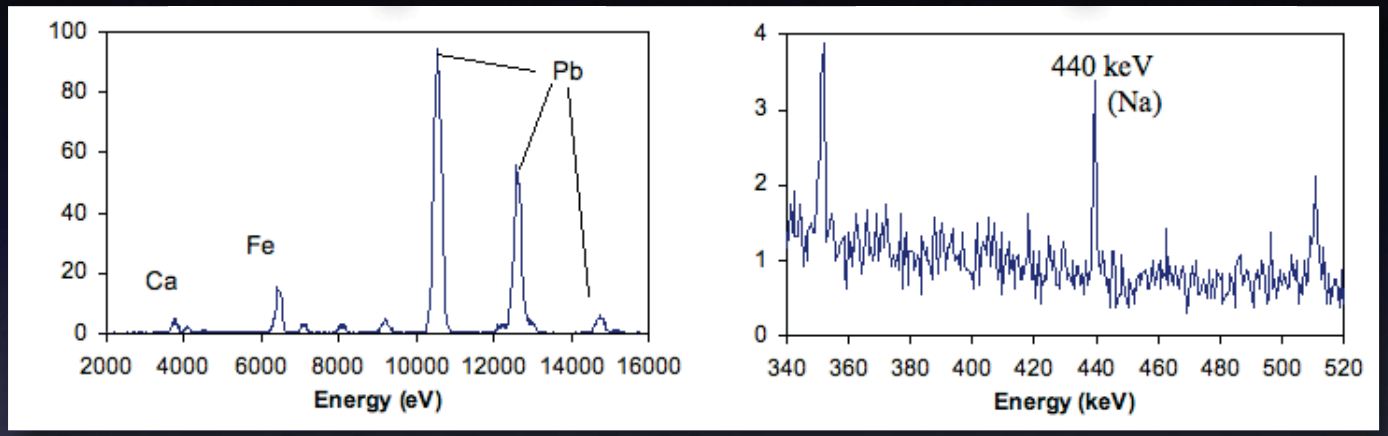

Restored

Cobalt blue and Zinc white (used only from XIX century!)

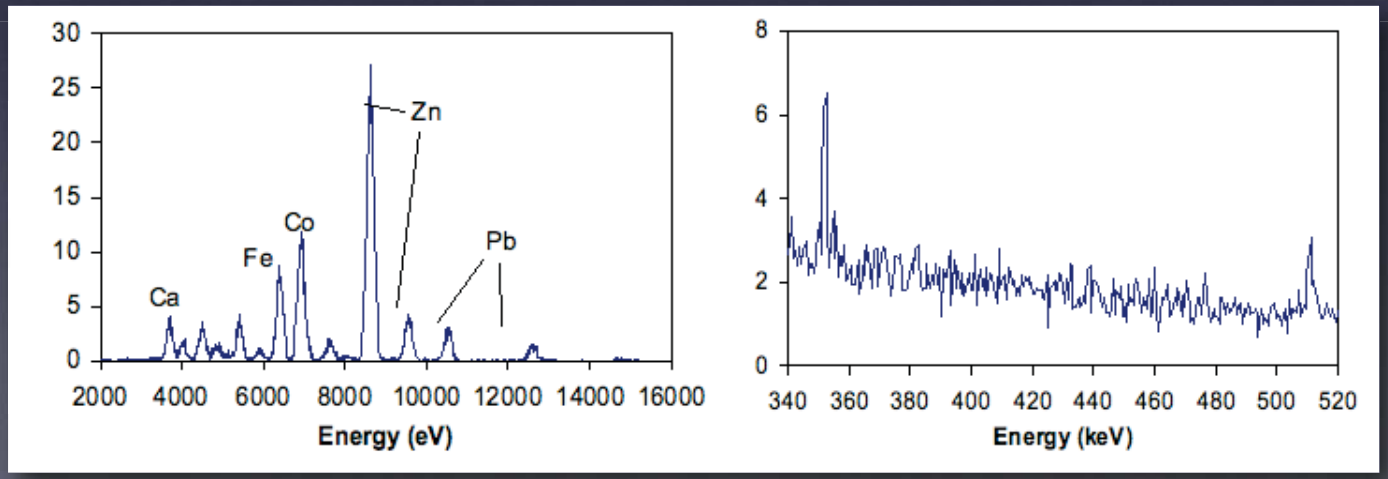

Analysis of lapis-lazuli artwork

Lapis-lazuli circle, embossed star made of yellow quartz

Rectangular box with carved faces, golden borders, base and feet

Little bowl with cusp shape cover, golden base and clasp

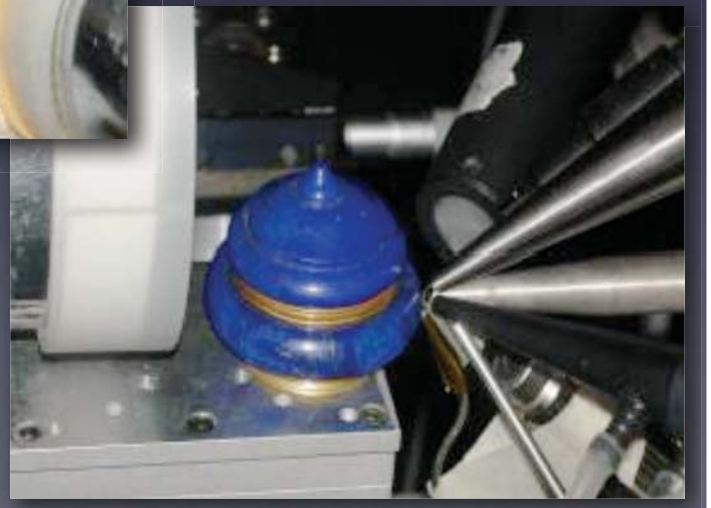

Analysis of lapis-lazuli artwork

Elemental maps from the "little bowl with cover"

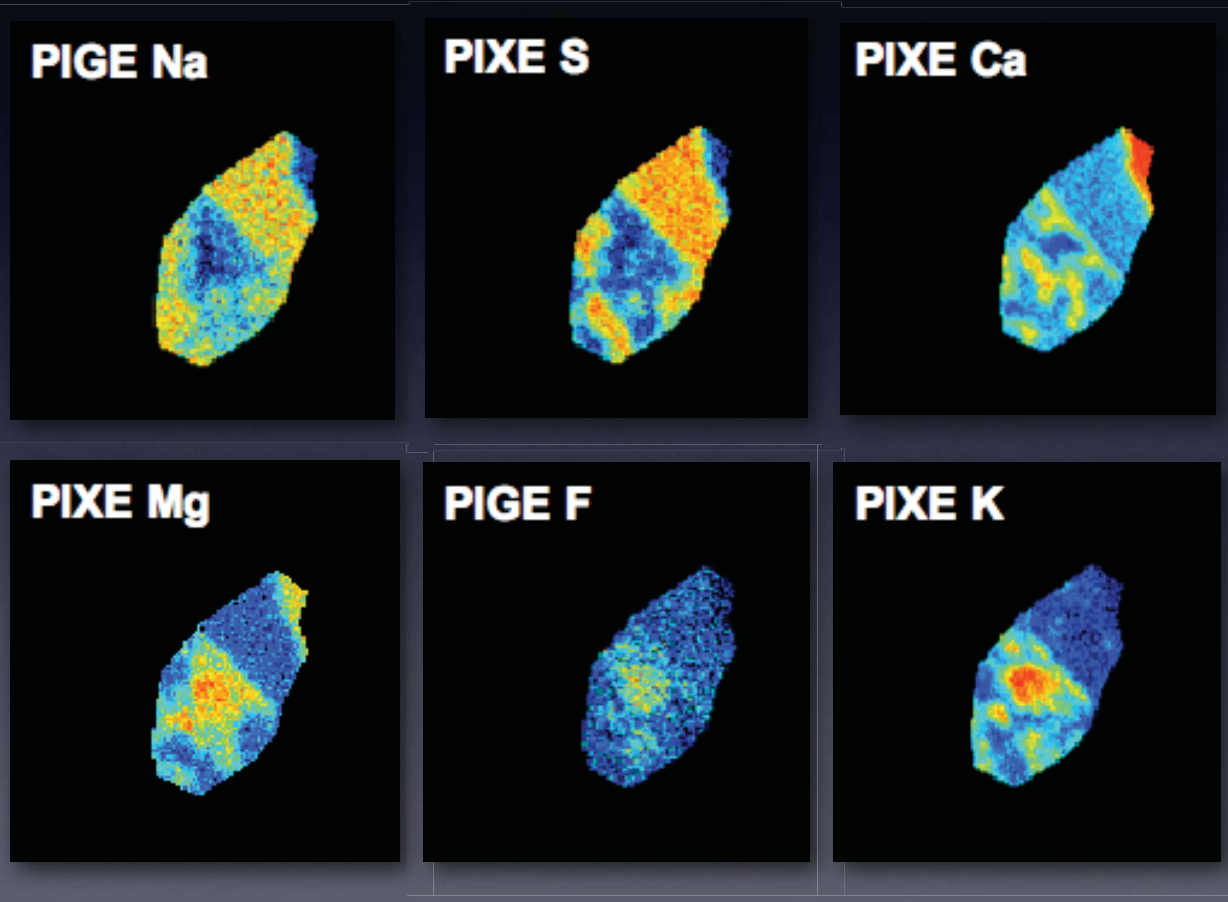

- Na and S: lazurite
- Ca and Mg: diopside
- F, K and Mg: phlogopite

Analysis of ancient Roman glasses

Quantification of sodium is of great importance for the characterisation of ancient glasses

Roman glass mosaic *tesserae* from Villa Adriana, Tivoli (Italy)

There are two basic typologies of Western glasses:

- **natron**
  (high Na_2O, low K_2O and MgO content)
  Roman and High Middle Ages
- **plant ash**
  (low Na_2O, high K_2O content)
  since Middle Ages

Sodium in Roman glasses

PIXE spectra — PIGE spectra

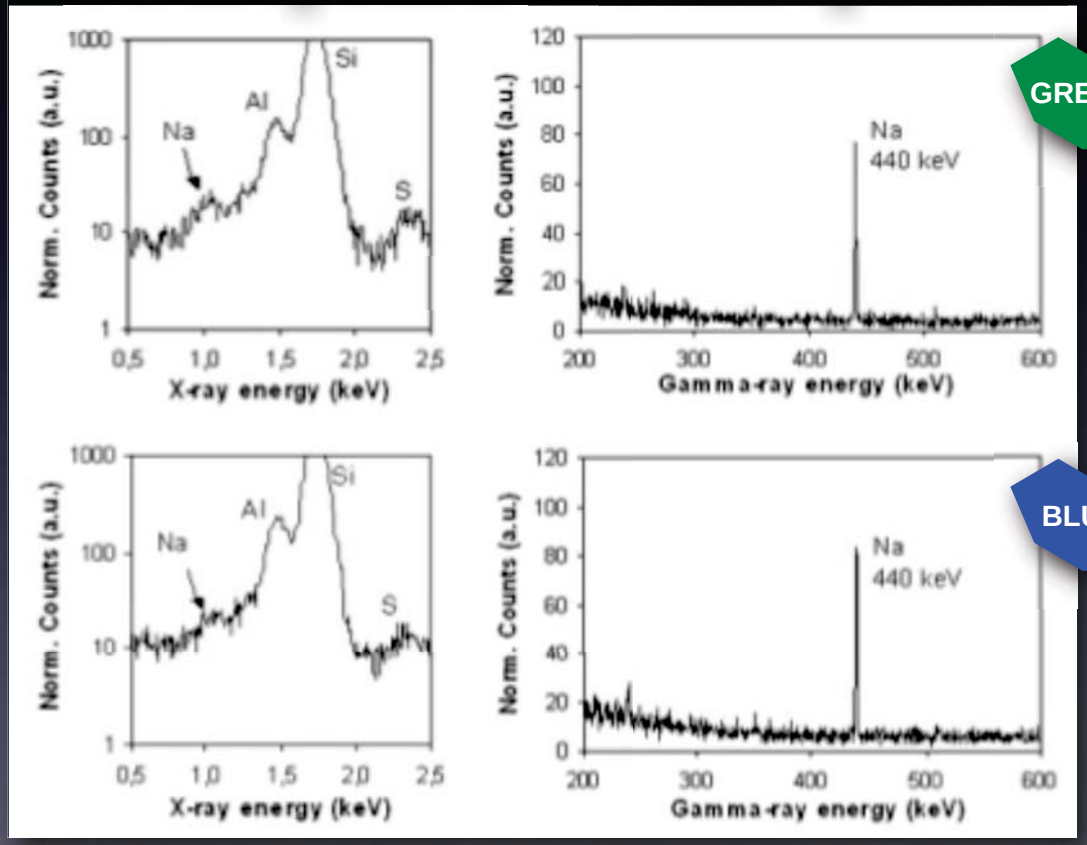

X-rays fom the lightest elements strongly absorbed by crusts and *patinae*

Sodium in Roman glasses

"freshly cut" zone

coloured but more opaque zone

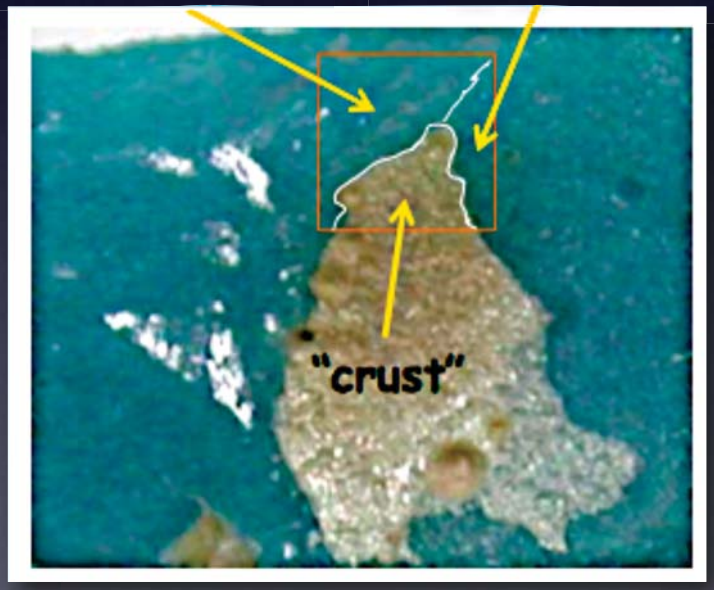

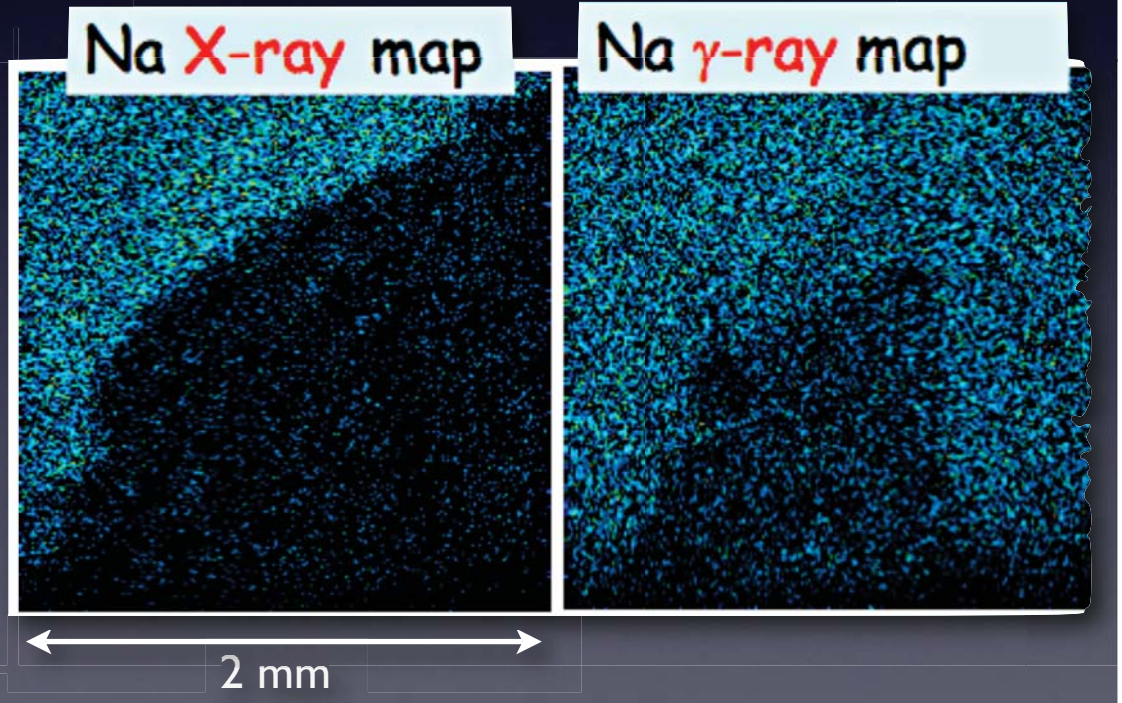

Sodium in Roman glasses

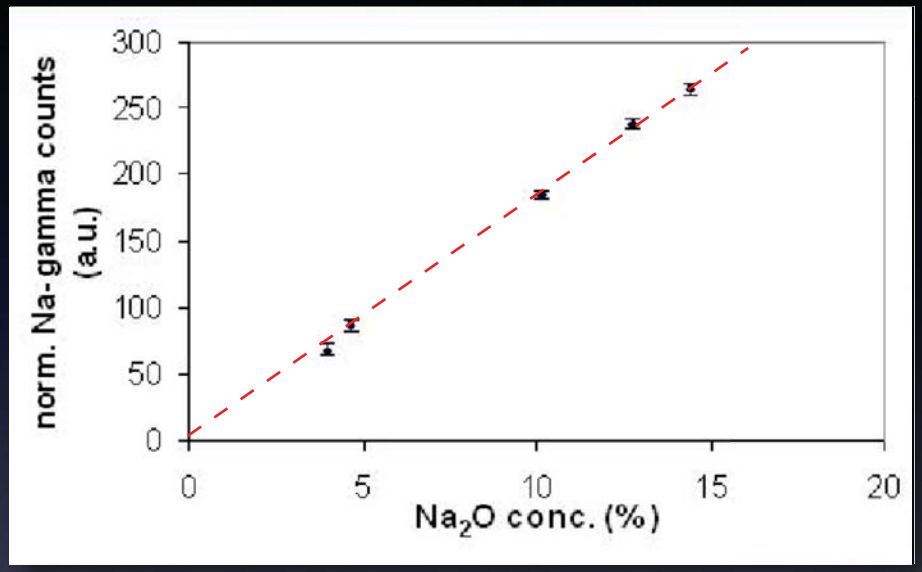

Estimate of Na content by comparing gamma-ray yields to those of thick glass standards (NIST SRM) with certified Na_2O concentration

Concentration ranges perfectly compatible with the typical Roman soda-lime-silica glass

glass colour	main oxides (%)			
	Na_2O	SiO_2	CaO	PbO
green	~20	55-60	5-9	1-3
blue	~20	60-65	5-9	<0.1
turquoise	~20	55-60	5-9	<0.3
yellow	~15	55-60	5-9	5-8
red	~10	35-40	5-9	30-35

Identification of corroded glass

The corrosion of glass implies the leaching of some elements (Ca, K, Na) from the interaction with moisture or water

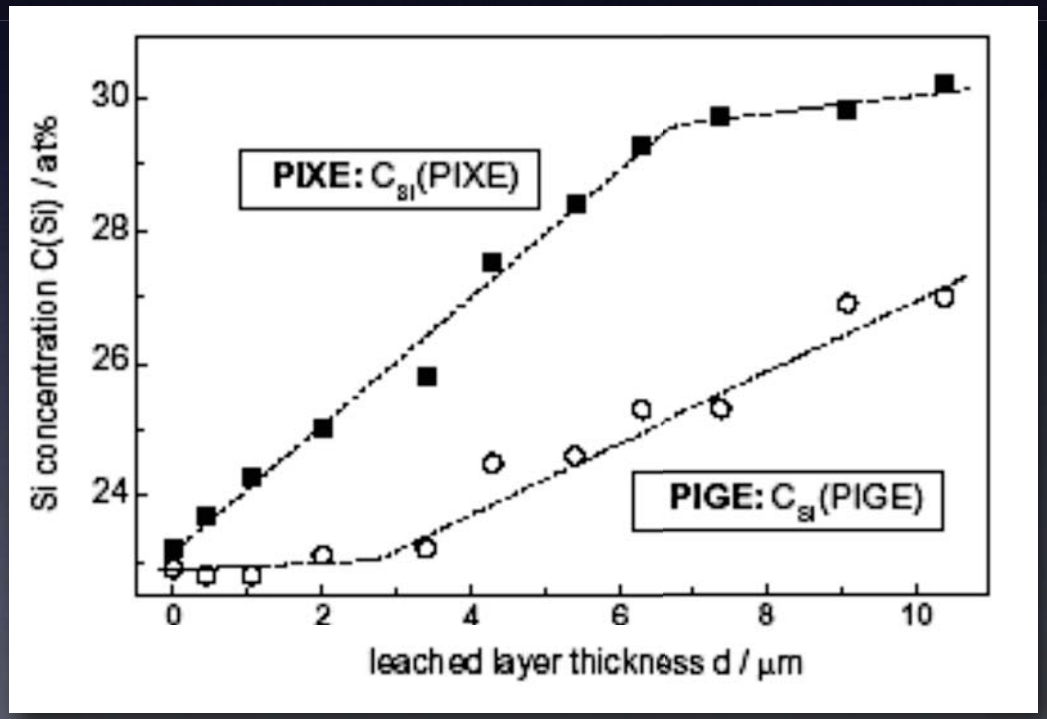

Formation of hydrate silicates on the surface

RBS study of glass corrosion

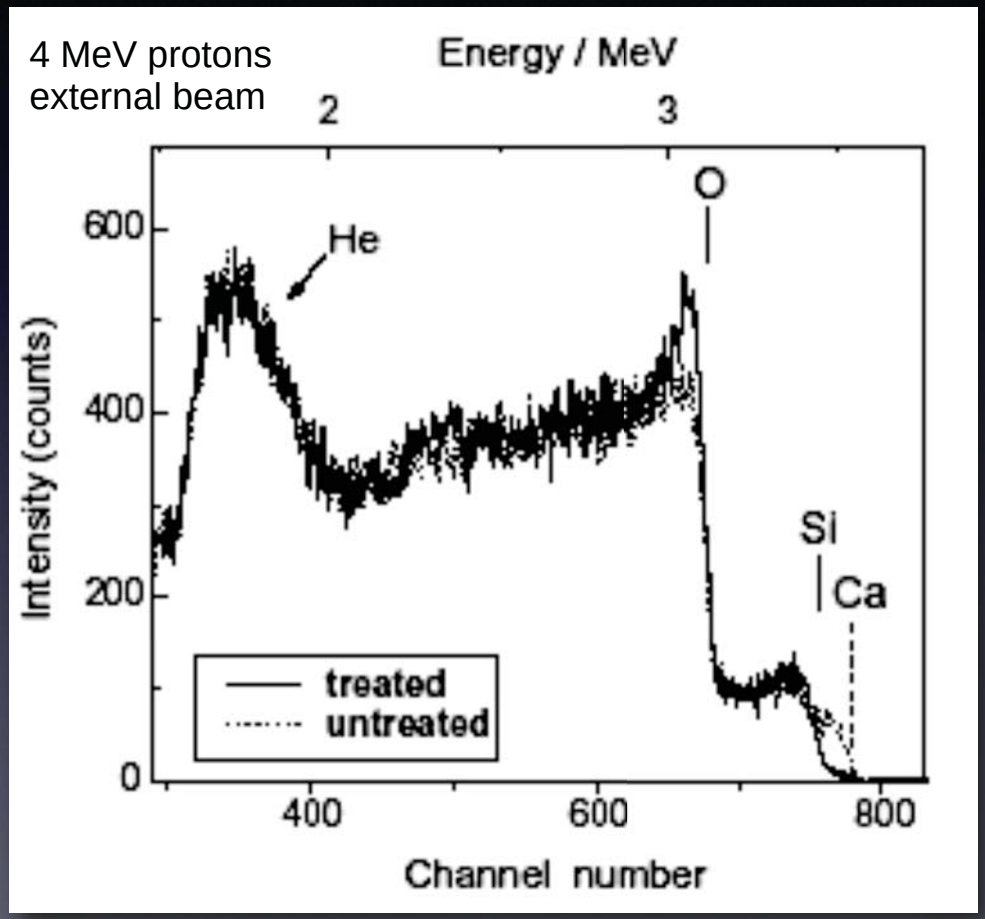

Leaching of Ca, K, Na from the interaction with moisture or water and formation of surface hydrate silicates

Differential PIGE

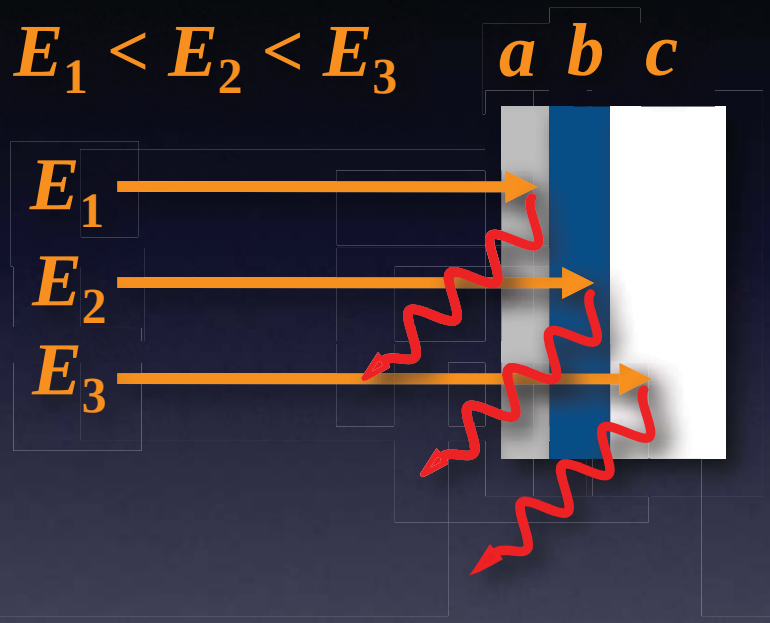

The principle of "Differential PIGE" (similar to Differential PIXE) is to compensate the intrinsic lack of depth resolution in PIGE bulk analysis by performing measurements at increasing beam energy in order to probe the sample composition at increasing depths (increasing ranges)

Example of Differential PIGE

Analysis of ancient glasses from Roman age.

Measurement with protons of energy from 1.6 to 5 MeV (each energy step corresponds to about 3.2 mg/cm^2).

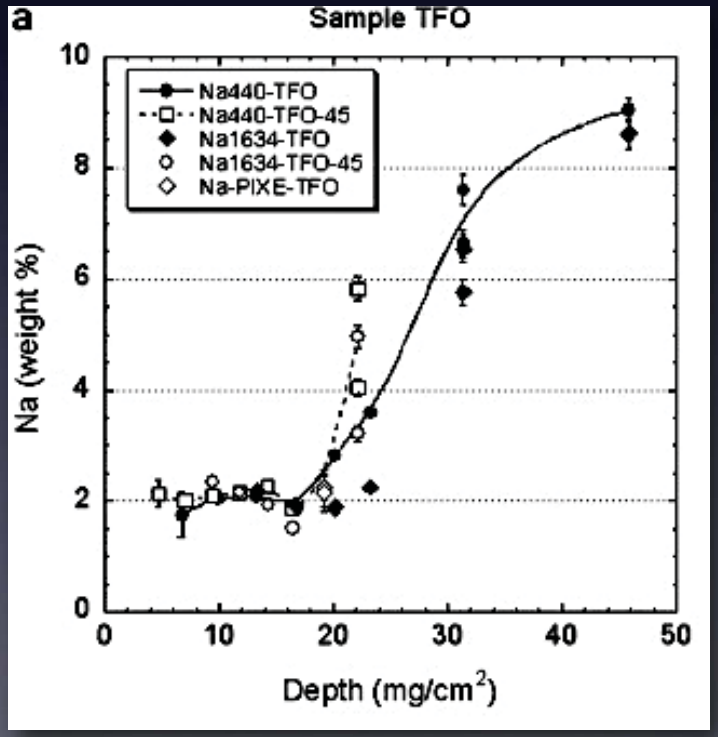

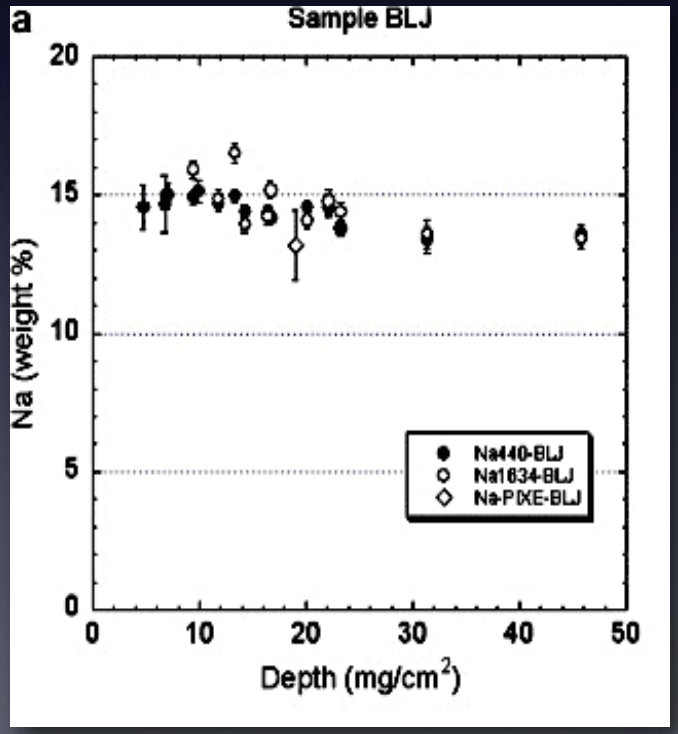

Surface alteration!

PIGE bulk analysis of thin targets

- Quantitative determination of light elements (F, Na or Al) with no self-absorption of emitted radiation inside the sample (i.e. analysis of aerosol particles)
- The unknown elemental concentrations are deduced by comparing the gamma-ray yields with those of a **thin** elemental standard
- Choosing the beam energy is crucial since the gamma emission cross sections have to be constant over the beam energy loss in the sample

PIGE bulk analysis of thin targets

Example: PIGE measurements can be used to correct the underestimation of PIXE due to low-energy X-rays absorption in the aerosol particles

Aerosol particles are a thin target (for 3 MeV protons ΔE is about 120 keV for "coarse mode" particles, i.e. PM10)

$$n_\gamma = n_p N \Delta\Omega \epsilon \int_{E_0-\Delta E}^{E_0} \frac{\mathrm{d}\sigma}{\mathrm{d}\Omega}(E,\theta)\frac{\mathrm{d}E}{S(E)}$$

If the PIGE cross sections are constant over the energy range ΔE then:

$$n_\gamma = n_p \sigma \Delta\Omega N t$$

The unknown concentrations can be deduce by comparing the gamma-ray yield to those of **thin** elemental standards

Quantitative PIGE analysis by comparison with thin elemental standards

Sample

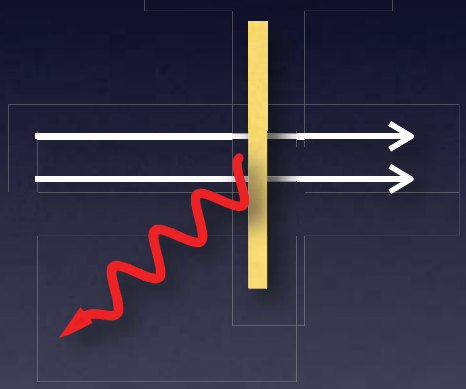

Standard

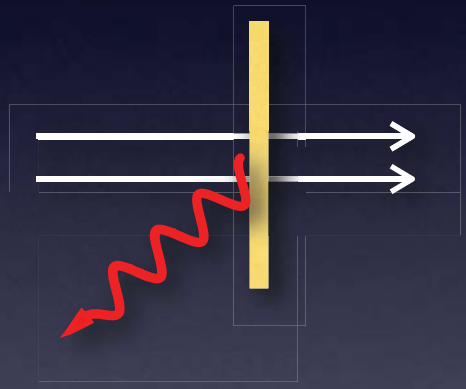

$$n_\gamma(Z)_{samp} = k_{Z,E} \cdot Q_{samp} \cdot (\rho_Z t)_{samp}$$

$$n_\gamma(Z)_{std} = k_{Z,E} \cdot Q_{std} \cdot (\rho_Z t)_{std}$$

$$(\rho_Z t)_{samp} = (\rho_Z t)_{std} \cdot [n_\gamma(Z)_{samp} / n_\gamma(Z)_{std}] \cdot (Q_{std} / Q_{samp})$$

Uncertainties in PIGE analysis

The experimental uncertainties on the elemental concentrations ($\mu g/cm^2$) measured by PIGE are given by the sum of independent uncertainties on:

- certified standard sample concentrations (5%)
- beam charge measurement (about 1%)
- peak areas; the uncertainty on peak areas includes the gamma-rays counting statistics and all the fitting uncertainties (background subtraction...). The counting statistics uncertainty may vary from few percent up to 20-30% or more when concentrations approach minimum detection limits (MDLs).

Spreading the beam for PIGE

- Finding energy intervals where prompt gamma-ray emission cross sections are **costant** and **high** enough.
- Prerequisite to provide an analytical method with good sensityvity and not affected by sample weight and matrix effects, suitable to large-scale analysis.
- Smooth the fluctuations in the PIGE cross sections (i.e. use a diffuser).

Use an external beam !

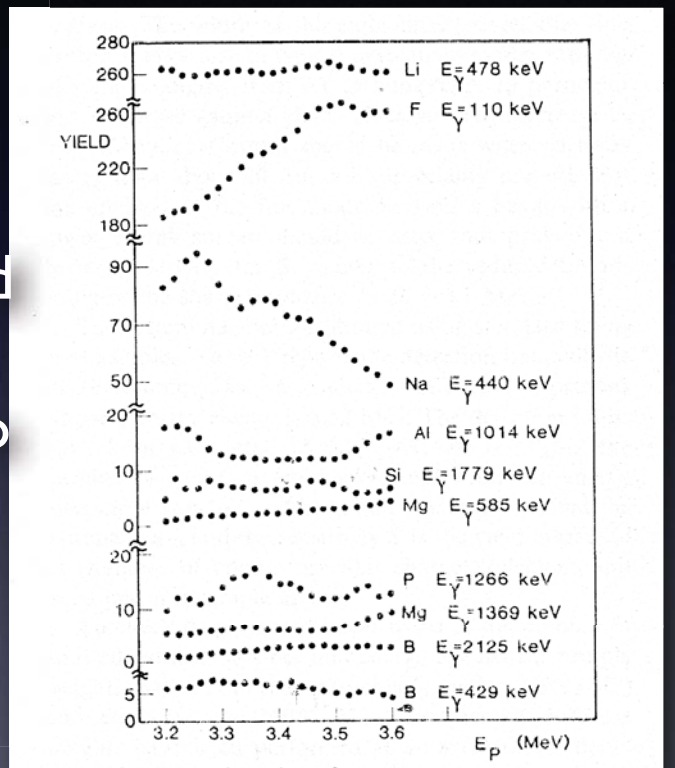

Fig. 1. Counts $\mu C^{-1} \mu g^{-1} cm^{-2}$ in the gamma peaks following reactions on Li, B, F, Na, Mg, Al, Si and P measured with an energy spread proton beam. The energy scale refers to the primary energy (see text).

C. Boni et al., NIM B 40/41, 1989

IBA with an external beam

Advantages

- direct analysis of filters having any shape and any size
- no sampling
- no charging, no preparation (conductive coating etc.)
- no heating, reduced damage risk
- easy sample positioning
- fast and efficient

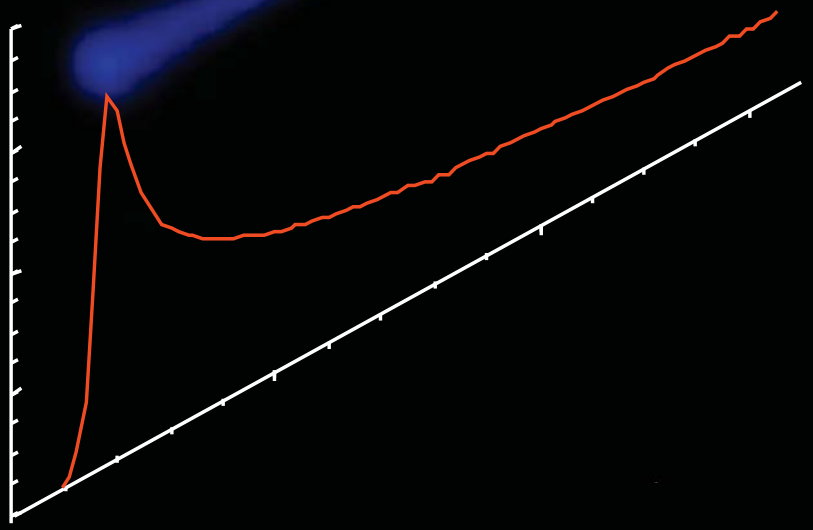

Disadvantages

- energy loss
- energy straggling
- beam lateral spread (bad for EBS)
- x-ray attenuation

Typical extraction windows

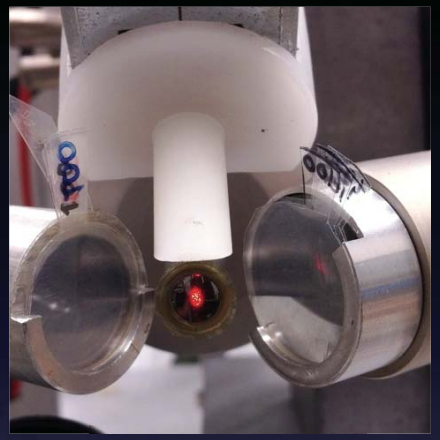

7.5 µm Upilex

0.5 µm Si_3N_4

Material	Thickness	Energy loss*	Energy straggling*, FWHM
Kapton/Upilex	7.5–8 **µm**	145 keV	20 keV
Si_3N_4	0.5 **µm**	40 keV	12 keV

* For 3 MeV protons, including the effect of 1 cm of He traversed by the beam before impinging on the sample

External beam PIGE yields

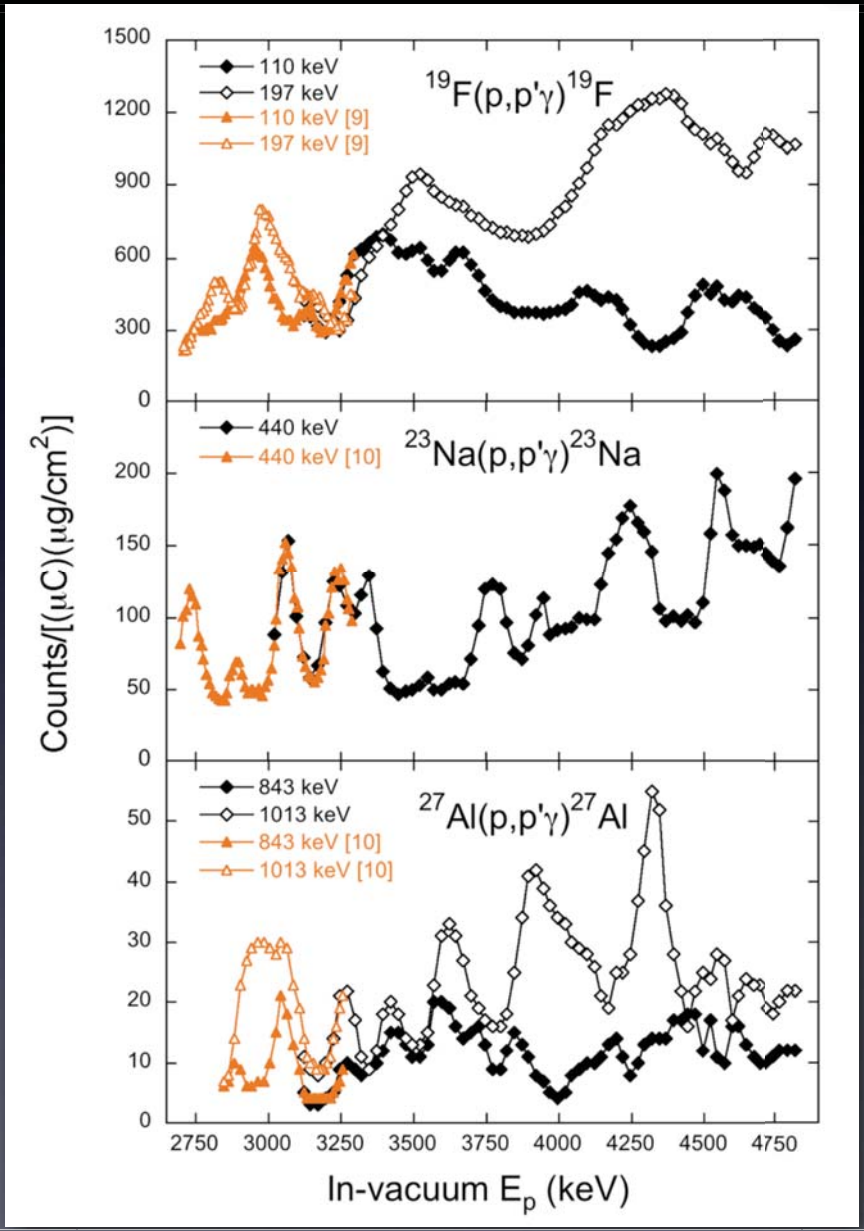

G. Calzolai et al., NIM B 268, 2010

Energy plateau region for PIGE

Reaction	E_γ (keV)	E_p (keV)	E_p on target[a] (keV)	Width (keV)	Average yield [counts/(μC·μg/cm^2)]
$^{19}F(p,p'\gamma)^{19}F$	110	4020	3863	175	380
		4395	4248	100	250
	197	3945	3785	125	700
		4420	4274	150	1250
$^{23}Na(p,p'\gamma)^{23}Na$	440	2990	2791	70	50
		3520	3346	100	50
		3670	3501	100	55
		4045	3889	75	90
		4470	4326	100	100
		4695	4556	100	150
$^{27}Al(p,p'\gamma)^{27}Al$	843	4370	4223	75	14
		4745	4607	75	10
	1013	3065	2870	120	29
		3820	3657	75	18
		4695	4556	75	23

[a] The proton beam energy E_p on target is calculated taking into account the energy loss in the 7.5 μm Upilex exit window and in the external path of 5 mm of air and 5 mm of He.

Energy plateau for Na measurement

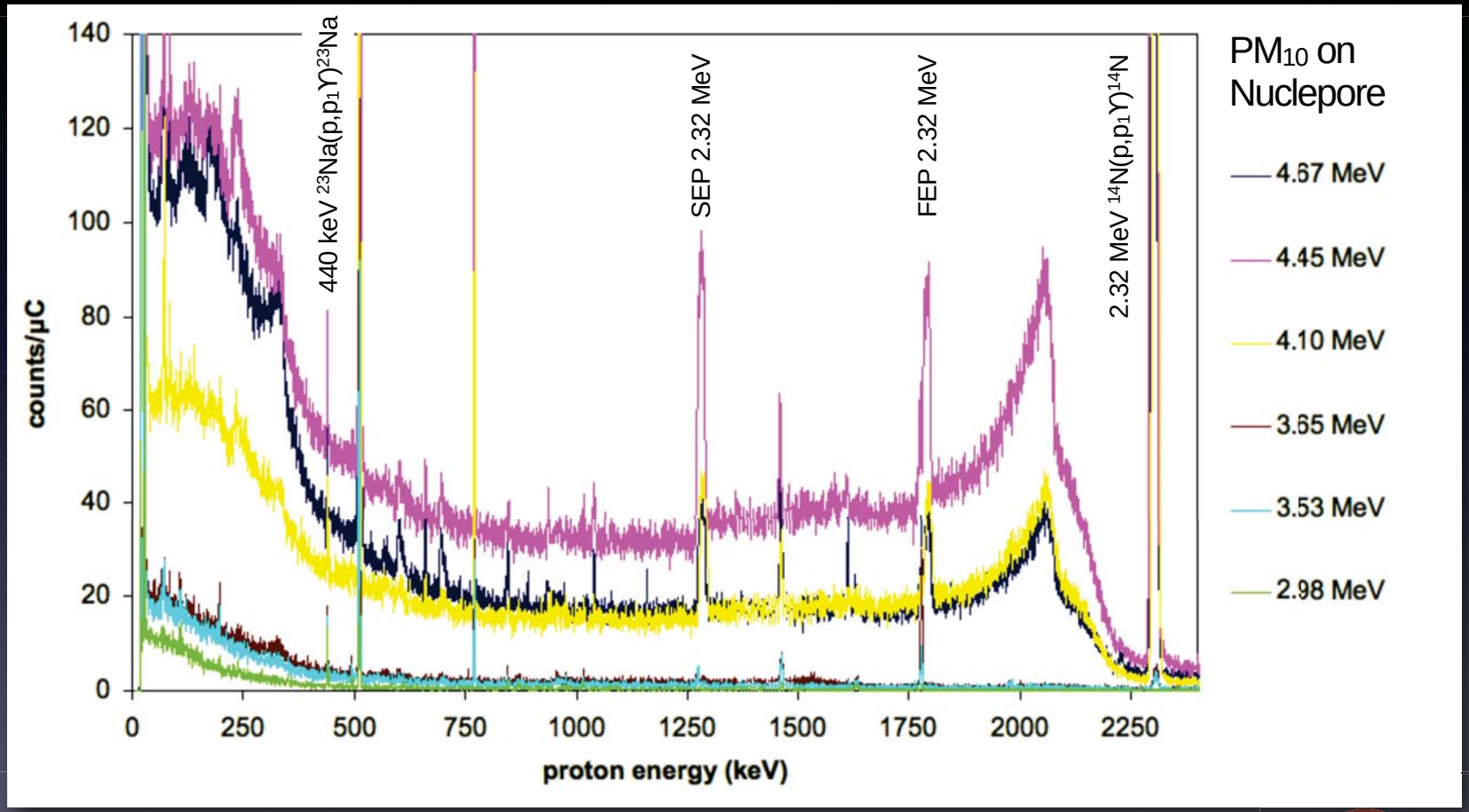

E_p (MeV)	4.67	4.45	4.10	3.65	3.53	2.98
MDL (ng/cm^2)	73	133	93	70	60	37

Measurement of Na in PM_{10} samples

Sampling site	E_P (keV)	PIGE (μg/cm^2)	PIXE (μg/cm^2)	PIXE/PIGE
Lampedusa (Re)	3520	19.6 ± 0.9	13.3 ± 0.2	0.68 ± 0.04
Lampedusa (Re)	3670	20.0 ± 0.8	13.3 ± 0.2	0.67 ± 0.03
Lampedusa (Re)	4045	20.7 ± 0.7	13.2 ± 0.1	0.64 ± 0.02
Lampedusa (Re)	4470	20.9 ± 0.8	13.3 ± 0.1	0.64 ± 0.03
Lampedusa (Re)	4695	20.8 ± 0.5	13.5 ± 0.2	0.65 ± 0.02
Sesto F.no (U)	4045	8.4 ± 0.6	5.5 ± 0.1	0.65 ± 0.05
Livorno (Ru)	4045	16.0 ± 0.6	11.2 ± 0.1	0.70 ± 0.03
Prato (T)	4045	7.3 ± 0.5	5.1 ± 0.1	0.69 ± 0.05

- PIGE reproducibility independent from the used plateau
- The self-absorption effects are almost the same for all the samples: Na concentration is underestimated by 30-35%

Measurements of Al in dust particles

Airborne mineral dust collected in-flight over Sahel desert

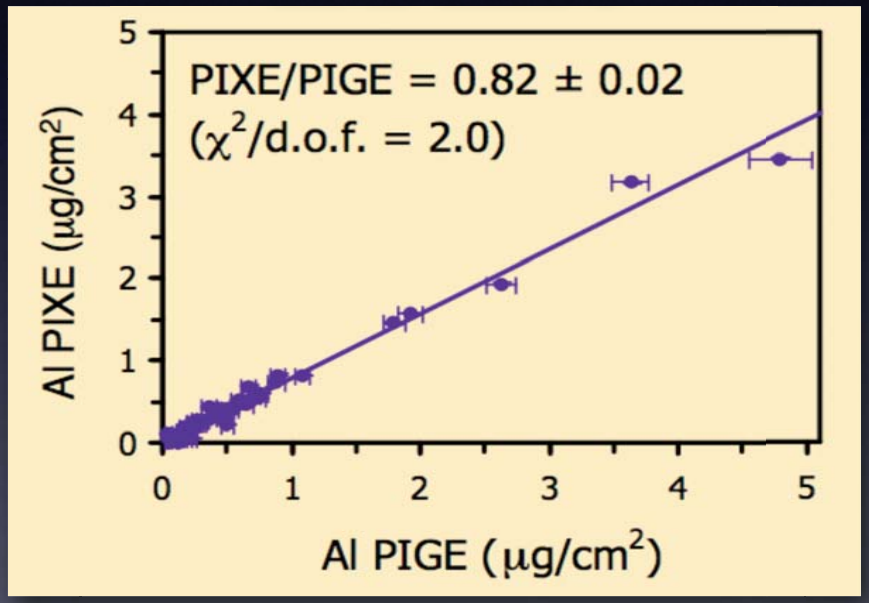

Mineral dust archived in Antarctic ice cores

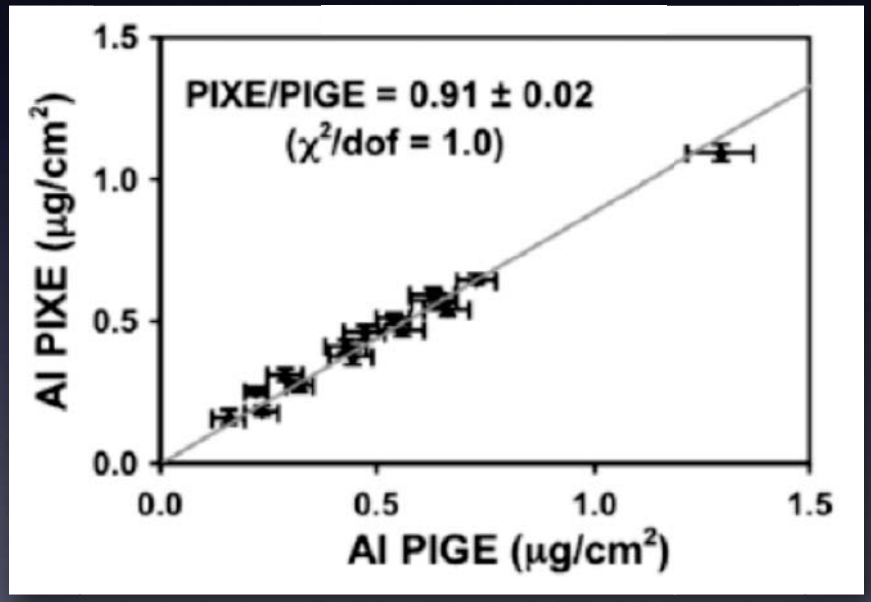

Correct the concentration of low-Z elements obtained by PIXE

Accurate study of geochemical composition of mineral dust

Study of geochemical composition of mineral dust

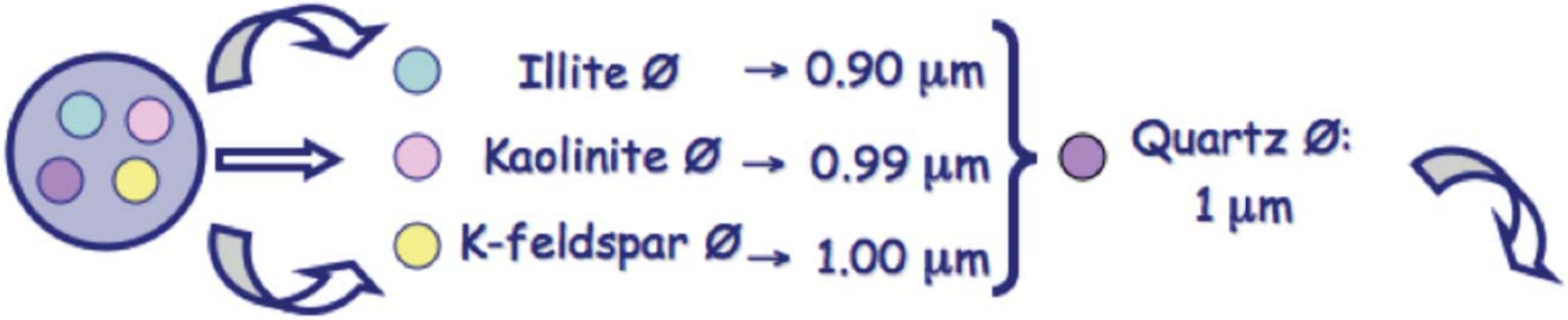

$$\left(\frac{PIXE}{PIGE}\right)^{Al}_{\substack{ice\\dust}} = 0.91$$

	Na	Mg	Al	Si	K
Kaolinite			0.91	0.90	
K-feldspar	0.79		0.91	0.92	0.97
Illite		0.87	0.91	0.91	0.97
Quartz				0.94	

$$AF = \frac{1 - \exp(-a \cdot D)}{a \cdot D}, a = \frac{2}{3} \cdot \mu \cdot \rho$$

B. Holynska and A. Markowicz, XRS 10, 1981

Scheme of the evaluation of the attenuation for the light elements in a dust sample, in the hypothesis that it is mainly composed by a mix of pure minerals, namely Kaolinite, Illite, K-feldspar and Quartz.

Study of desert aerosol composition

Mineral dust is one of the major components of atmospheric aerosols (~40% on a global scale): it has important effects on the radiative budget of the atmosphere and thus on climate change.

Estimates of the global mean direct radiative forcing by mineral dust vary in a wide range (+0.09 to –0.46 W/m^2), owing to uncertainties in the mineralogical composition and size distribution.

An accurate quantitative analysis of airborne dust is needed.

Study of desert aerosol composition

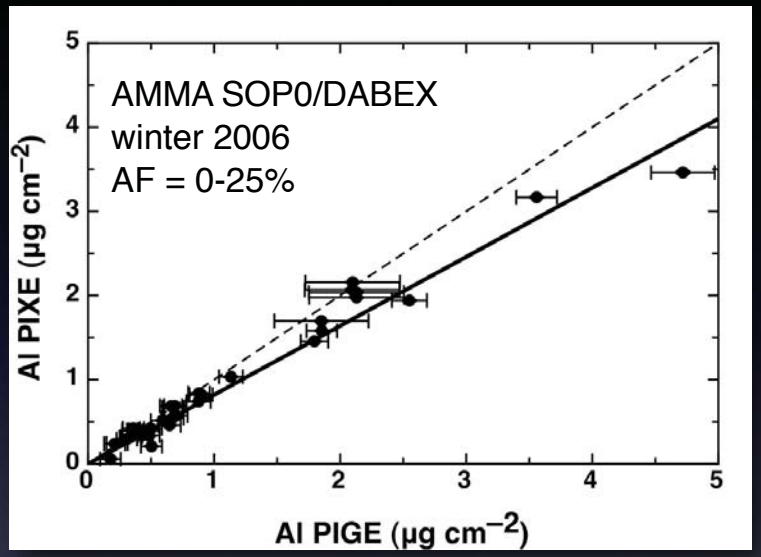

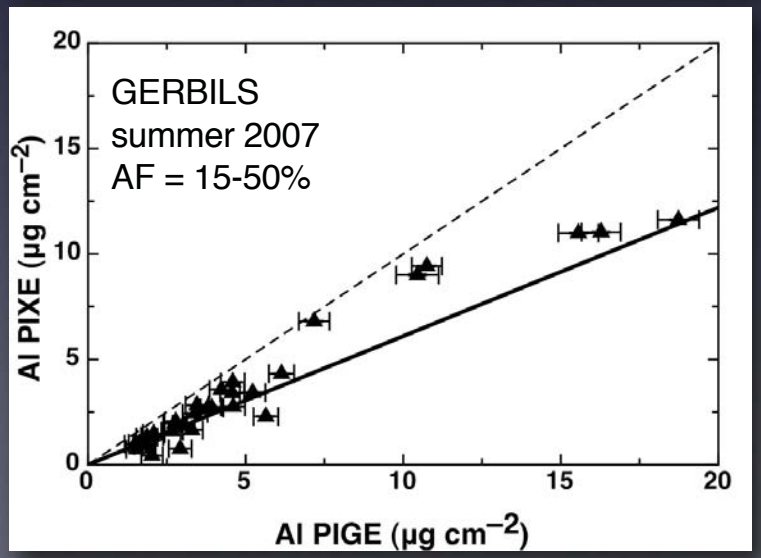

- Airborne aerosols collected in flight over the Sahel desert during two sampling campaigns
- In winter, the collected dust originated from northern Africa and was transported towards the sampling area in well defined "plumes"
- In summer, the dust was more frequently produced locally over the Sahel by erosion processes
- The average size distributions were indeed expected to be different: in summer the dust is more enriched in coarse particles than in winter

Fingerprinting the desert dust

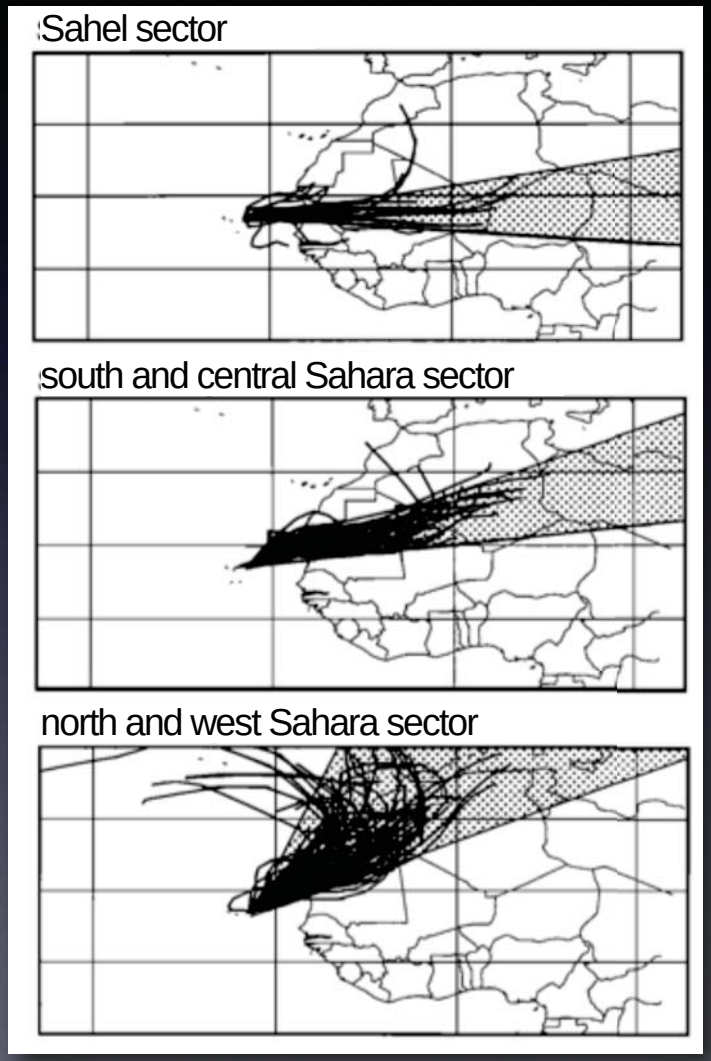

- Interelemental ratios in mineral dust measured at a receptor site can be used to differentiate source regions.

Table 1. Elemental Ratios of Dust Collected at Sal According to the Sectors of Origin Presented in Figure 2*

	Sector 1	Sector 2	Sector 3
Si/Al			
Mean	2.03	2.21	2.32
s.d.	0.09	0.07	0.10
Ca/Al			
Mean	0.20	0.36	0.60
s.d.	0.05	0.07	0.19
Fe/Ca			
Mean	2.71	1.43	0.90
s.d.	0.59	0.32	0.30
K/Ca			
Mean	0.96	0.62	0.43
s.d.	0.21	0.10	0.11

- If not corrected, elemental ratios prevent the possibility of distinguishing the origin of the dust.

I. Chiapello et al., J. Geophys. Res. 102, 1997

Study of ice core dust composition

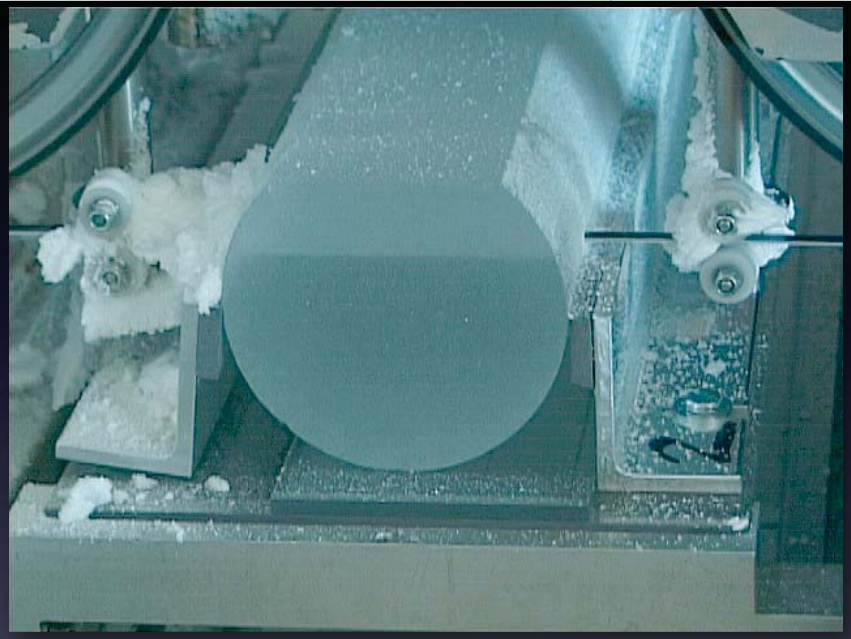

EPICA ice core (lenght 3190 m).
Ice sampled to an age of 800 kyr BP.

Polar ice cores are extensive archives of records of past atmospheric compositions, allowing paleoclimate research.

Snow, accumulated and compressed into solid ice, contains traces of the gases and the aerosols being in the atmosphere at the deposition time.

No post-depositional processes affect dust.

Study of ice core dust composition

Italian-French "Station Concordia" at Dome C.

No local dust sources in Antarctica.

Dust particles reach the inner Antarctic areas after long-range transport from continental areas in Southern Hemisphere.

From the analysis of the geochemical composition of ice core dust it is possible to infer the dust source location.

Ice core and PSA dust composition

The study of the composition of dust particles deposited over the Antarctic ice sheet and archived in ice core samples (spanning the last 220 kyr) helps to investigate global climate changes (EPICA project)

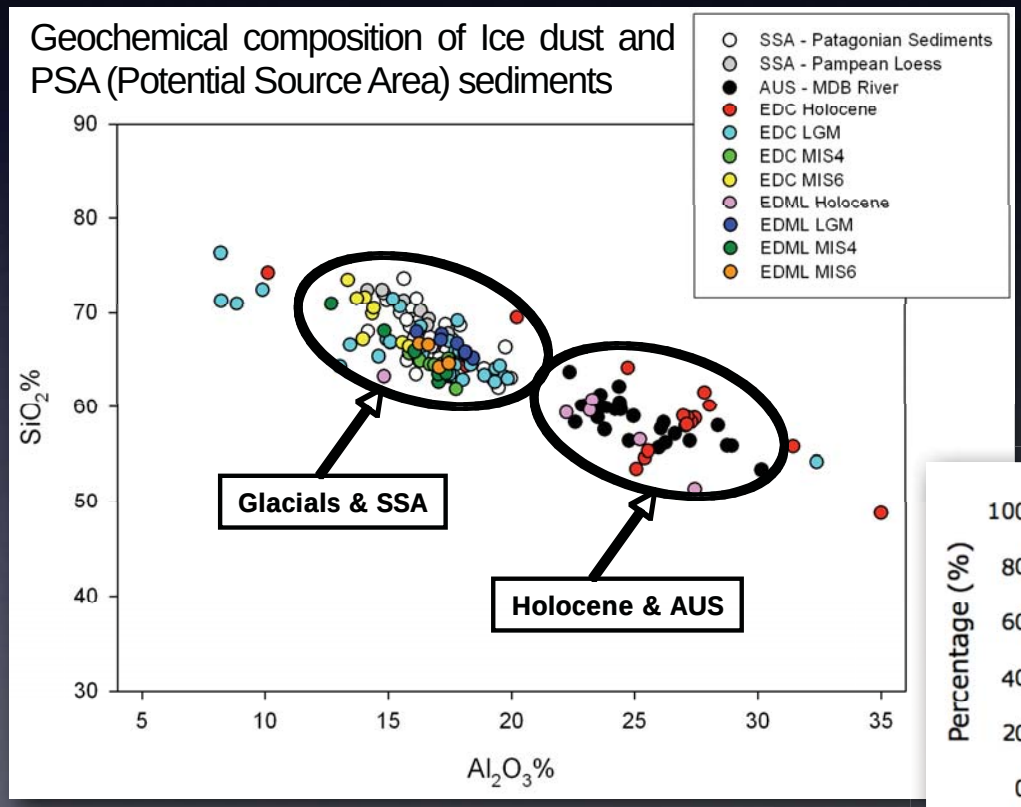

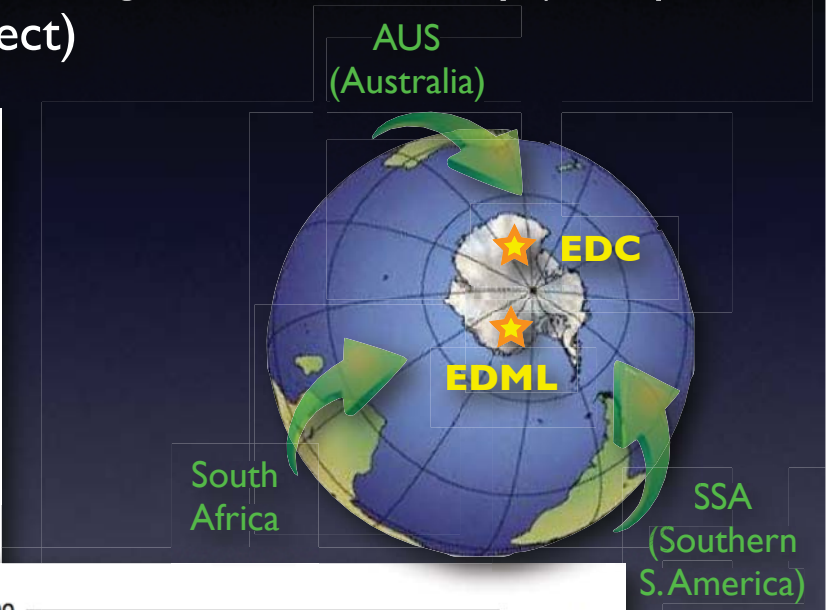

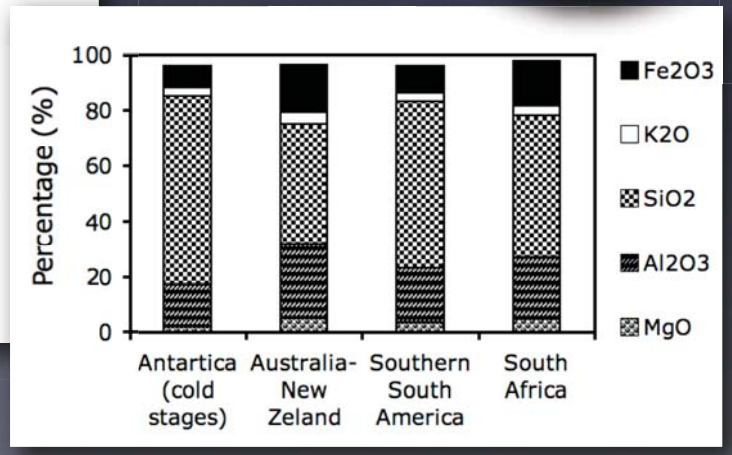

F. Marino et al., Geophys. Res. Lett. 36, 2009

PIGE depth profiling

Resonance depth profiling

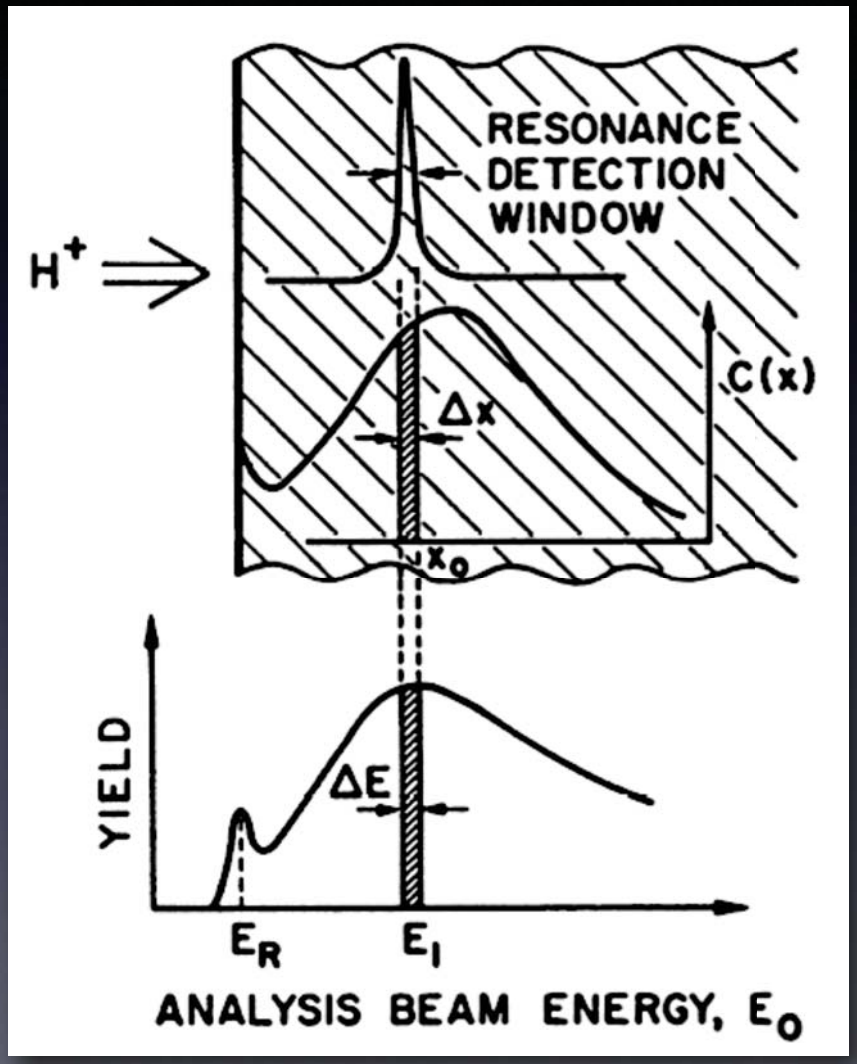

Scanning the sample composition as a function of depth, "moving" a resonance inside the sample by changing the incident beam energy

Depth scale:

$$x = (E_0 - E_R) / S(E)$$

Excitation curve

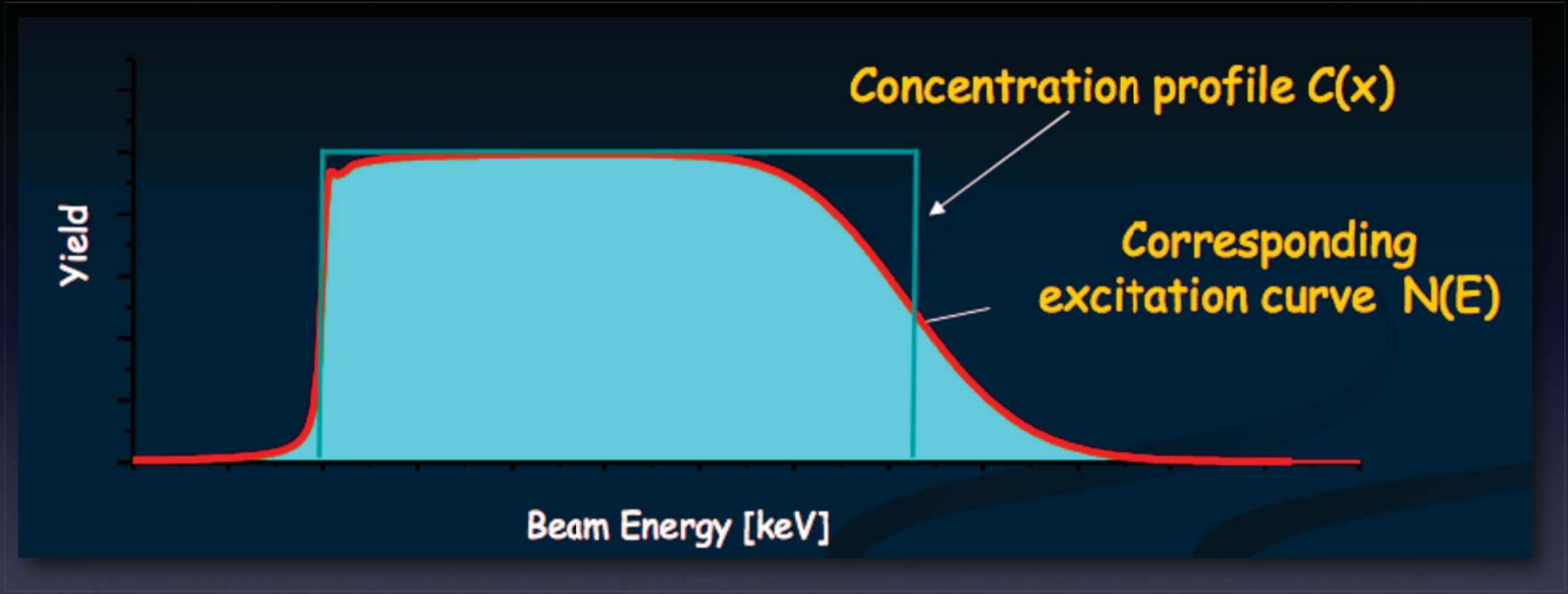

$$N(E) = G(E) * \Gamma(E) * T(E) * C(x)$$

$G(E)$ beam + Doppler energy spread
$\Gamma(E)$ resonance lineshape
$T(E)$ beam energy straggling

Lewis effect (Lewis peak)

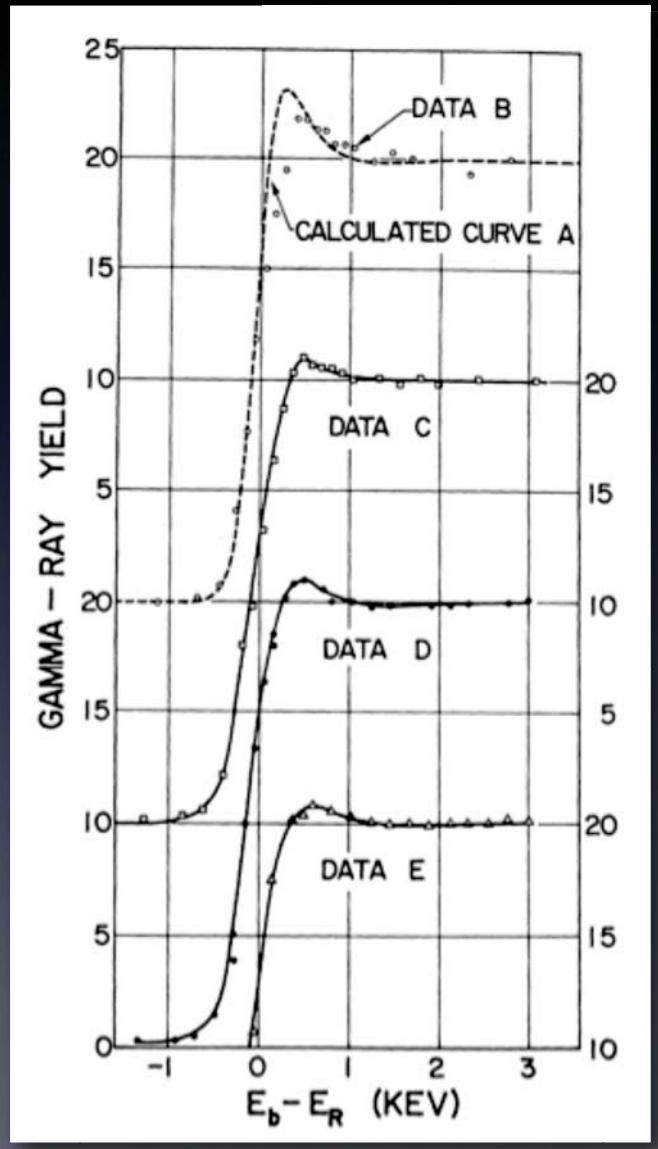

Manifestation of the quantum nature of the energy loss process as the ion slows down during its passage through the target.

"In passing through target material a charged particle loses energy in discrete steps Q. If some of these steps are larger than the natural width of a narrow resonance, some of the particles incident on a target at an energy well above the resonance energy, E_R, will jump over the resonance. If particles are incident at E_R then all will have for a finite time the correct energy to interact. The yield curve should therefore exhibit a peak near E_R"

H.W. Lewis (private communications, 1960-61)

Reactions for resonant PIGE with protons

Element	Reaction	E_r (keV)	Γ_r (keV)	E_γ (MeV)
Li	$^{7}Li(p,\gamma)^{8}Be$	441.4	10	17.7, 14.7
B	$^{11}B(p,\gamma)^{12}C$	163	5.2	4.43
C	$^{13}C(p,\gamma)^{14}N$	1748	0.075	9.17
N	$^{14}N(p,\gamma)^{15}O$ $^{15}N(p,\alpha\gamma)^{12}C$	1059 429	3.9 0.12	8.3, 5.2, 3.0 17.7, 14.7
O	$^{18}O(p,\gamma)^{19}F$	1167	0.05	6.3, 2.6
F	$^{19}F(p,\alpha\gamma)^{16}O$	340.5	2.4	6.1
Na	$^{23}Na(p,\alpha\gamma)^{20}Ne$	1011	<0.1	1.63
Mg	$^{26}Mg(p,\gamma)^{27}Al$	1548	0.020	9.8, 8.7, 7.6
Al	$^{27}Al(p,\gamma)^{28}Si$	991.9	0.10	10.8, 1.78
Cr	$^{52}Cr(p,\gamma)^{53}Mn$	1005		2.5-4.7

Reactions for resonant PIGE with alphas

Element	Reaction	E_r (keV)	Γ_r (keV)	E_γ (MeV)
Li	$^{7}Li(\alpha,\gamma)^{11}B$	953	4	9.7, 4.8, 4.4, 2.53
B	$^{10}B(\alpha,p\gamma)^{13}C$	1507 1645	25 22	3.85, 3.68
N	$^{14}N(\alpha,\gamma)^{18}F$	1531	<0.1	4.52, 2.47, 1.08
Ne	$^{20}Ne(\alpha,\gamma)^{24}Mg$	1929		9.56

Depth resolution

$$\delta x = \sigma_{TOT}(x) / S(x)$$

$$\sigma^2_{TOT}(x) = \sigma^2_b + \sigma^2_D + \sigma^2_{surf} + \Gamma^2_r + \sigma^2_{str}(x)$$

σ_b beam ernergy resolution

$\sigma_D = (2 \cdot M_1 \cdot E_0 \cdot kT / M_2)^{½}$ Doppler broadening due to target atom vibrations

$\sigma_{surf} = \sigma_x \cdot S(E)$ sample surface roughness (σ_x)

Γ_r resonance width

$\sigma_{str}(x)$ beam energy straggling

Depth resolution

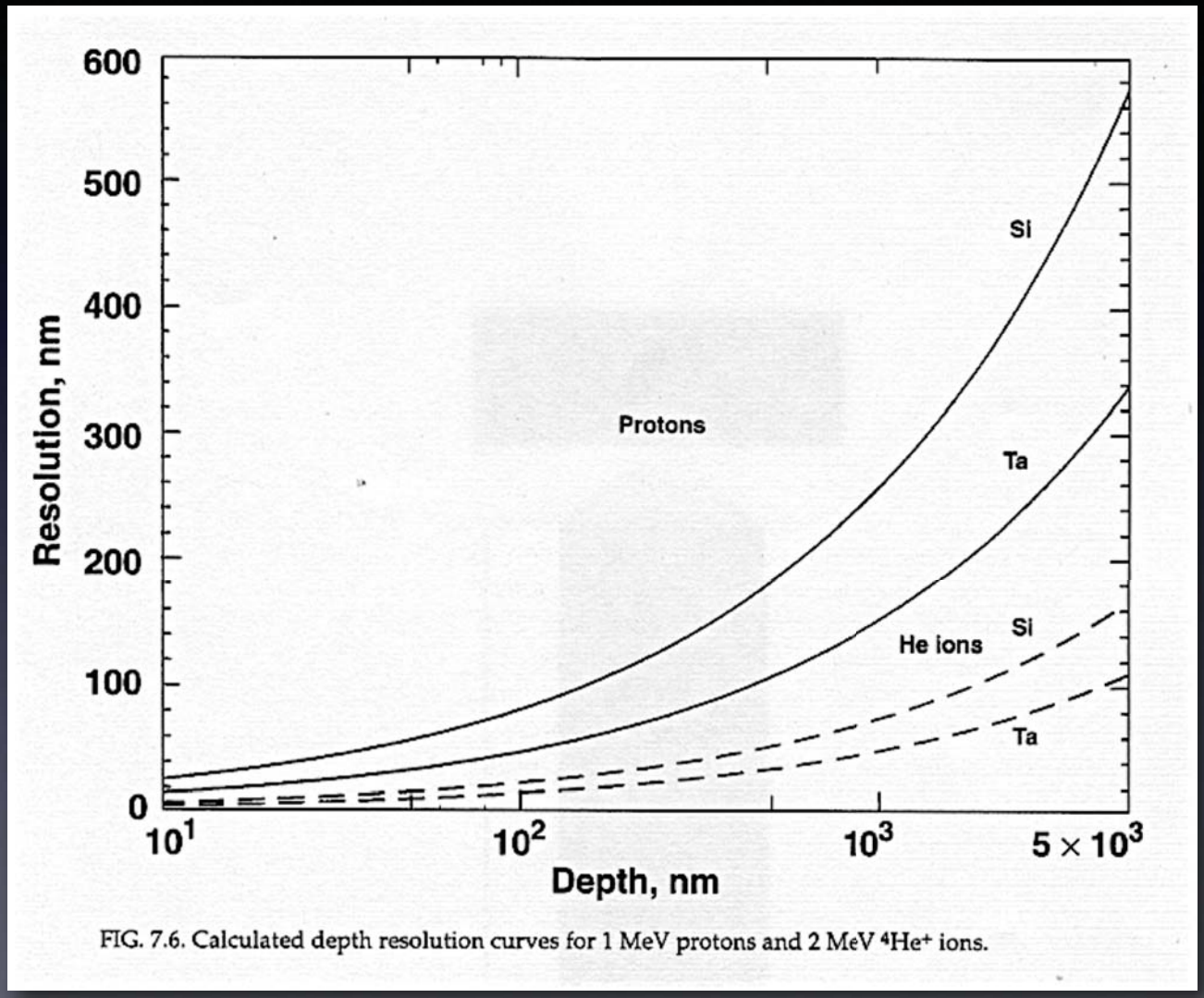

FIG. 7.6. Calculated depth resolution curves for 1 MeV protons and 2 MeV $^4He^+$ ions.

Resonance H depth-profiling

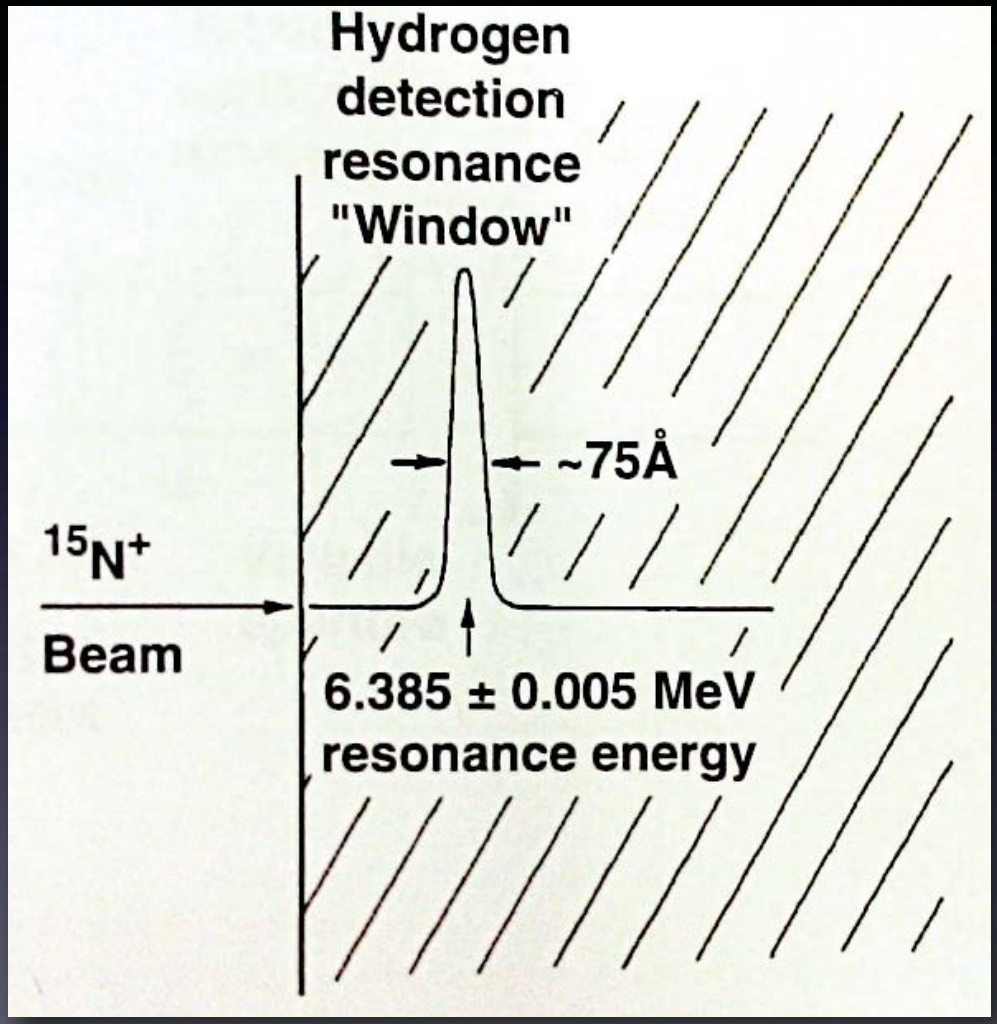

$^{1}H(^{15}N,\alpha\gamma)^{12}C$, E_γ = 4.43 MeV

Resonance H depth-profiling

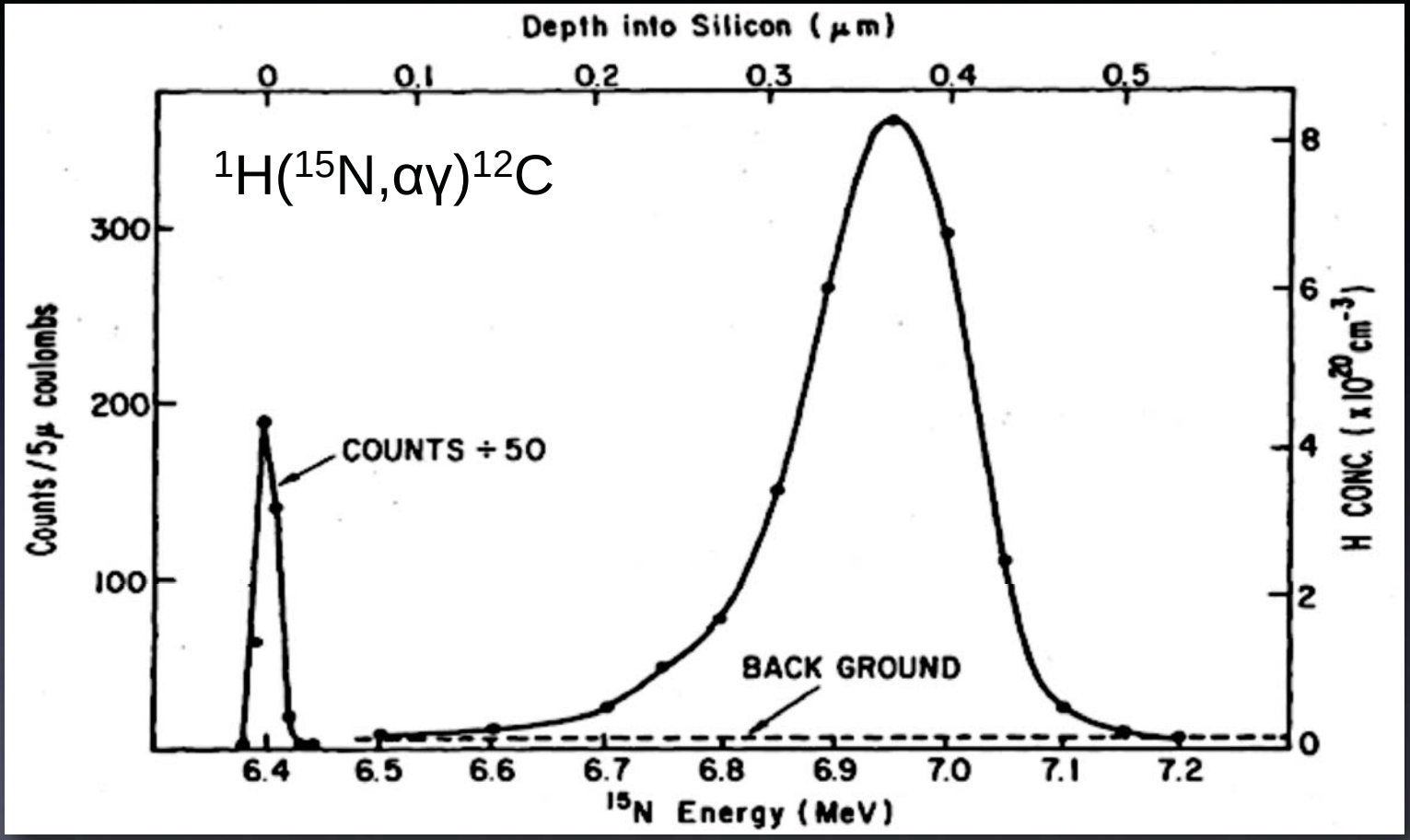

Measurement of the implantation profile of H (10^{16} at/cm^2, 40 keV) in Si

Resonance H depth-profiling

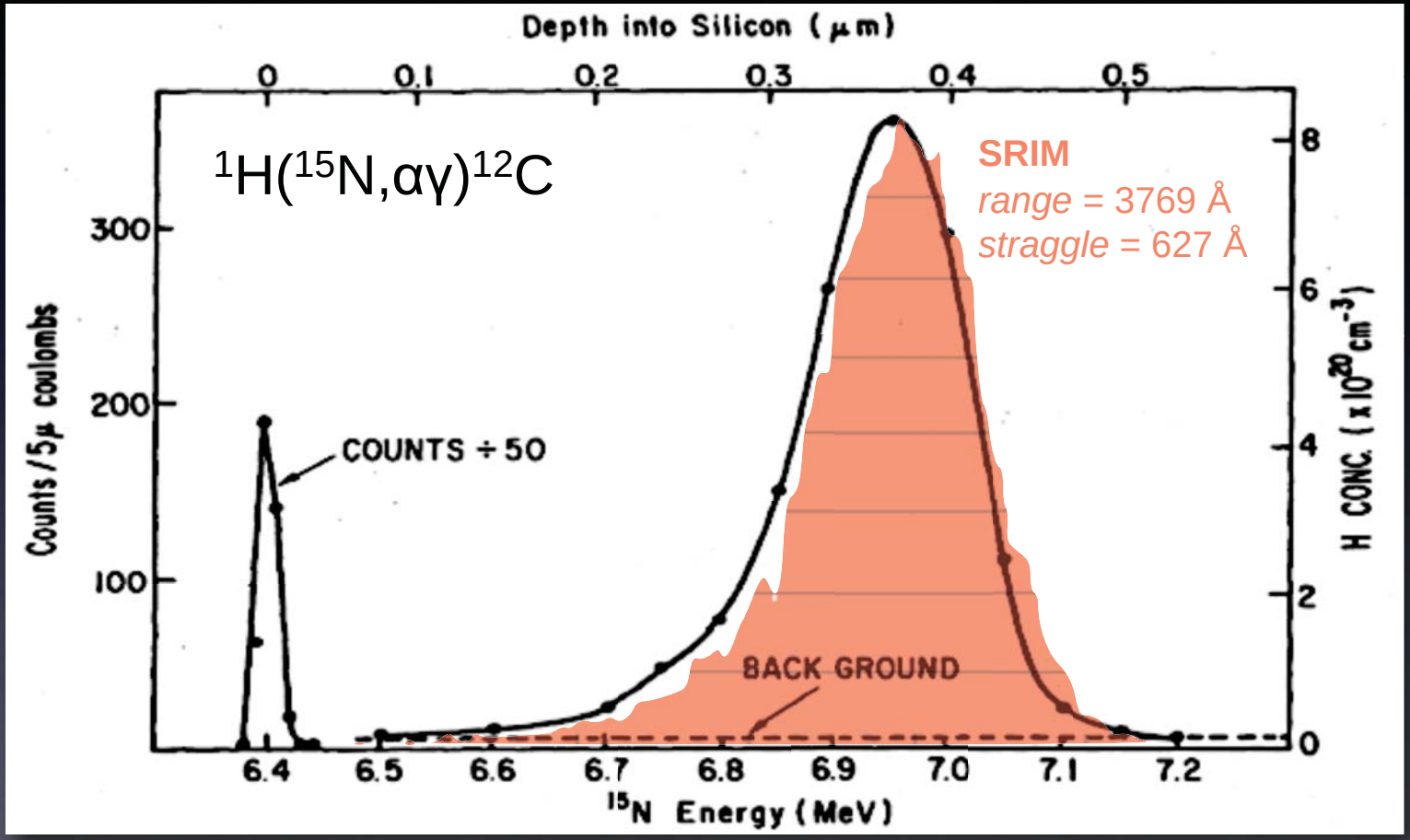

Measurement of the implantation profile of H (10^{16} at/cm^2, 40 keV) in Si

Resonances for H depth-profiling

Reazione	E_r (MeV)	Γ_r (keV)	$\sigma(E_r)$ (mbarn)	E_γ (MeV)	next E_r (MeV)
$^{1}H(^{7}Li,\gamma)^{8}Be$	3.07	81	4.8	17.7, 14.7	7.11
$^{1}H(^{15}N,\alpha\gamma)^{12}C$	6.385 13.35	1.8 25.4	1650 1050	4.43	13.35 18.0
$^{1}H(^{19}F,\alpha\gamma)^{16}O$	6.418 16.44	44 86	88 440	6.13, 6.98, 7.12	9.1 17.6

Interferences from next resonances

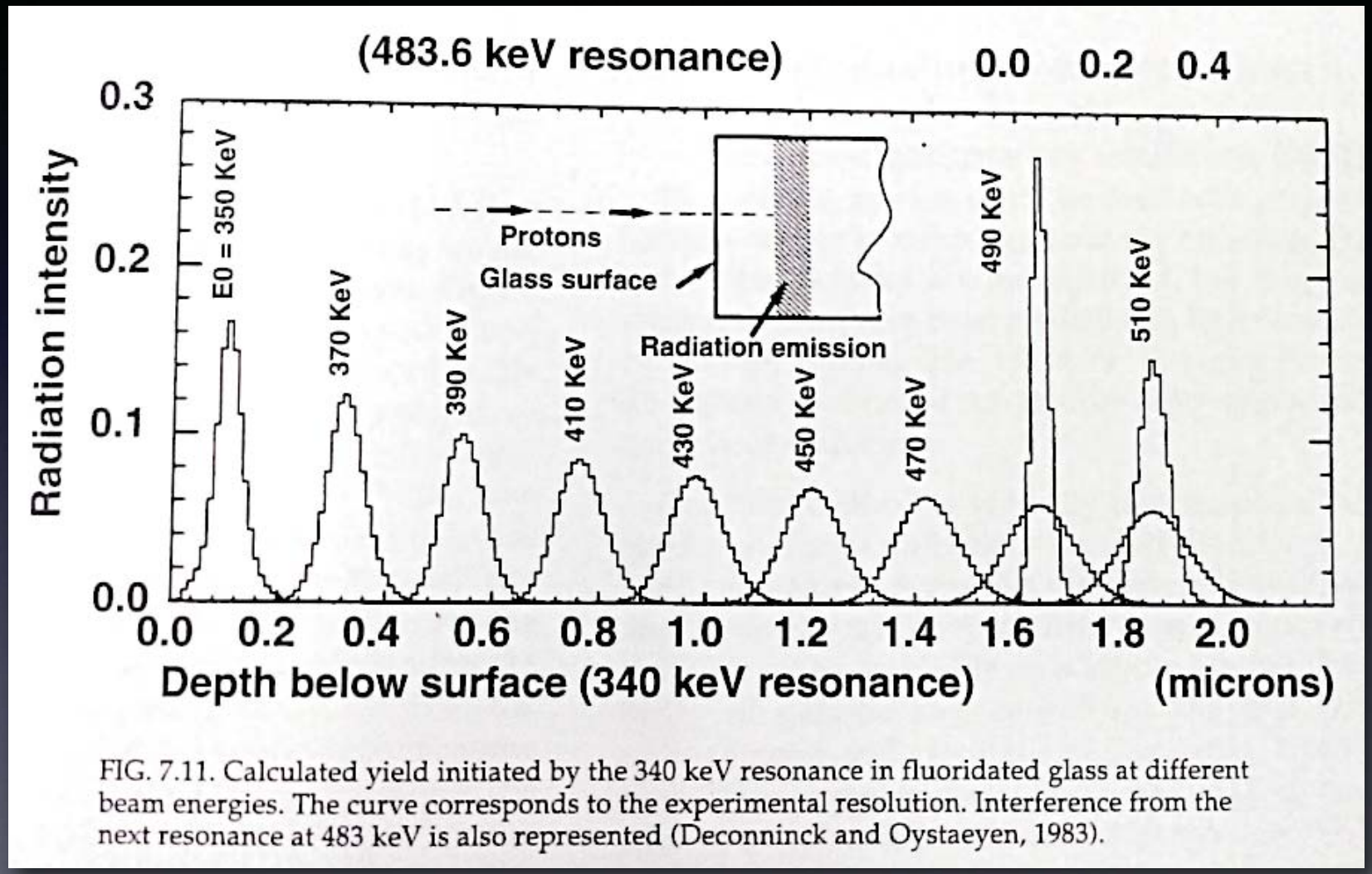

FIG. 7.11. Calculated yield initiated by the 340 keV resonance in fluoridated glass at different beam energies. The curve corresponds to the experimental resolution. Interference from the next resonance at 483 keV is also represented (Deconninck and Oystaeyen, 1983).

$^{19}F(p,\alpha\gamma)^{16}O$, E_γ = 6-7 MeV

Thanks for
your attention!

Essential bibliography

- Y. Wang, M. Nastasi ed.s *"Handbook of Modern Ion Beam Materials Analysis"* MRS
- G. Deconninck et al. *"Prompt gamma-ray spectroscopy and its use in elemental analysis"* At. Energy Rev. suppl. no. 2 (1981) 151
- G.F. Knoll *"Radiation Detection and Measurements"* John Wiley & Sons